UNIVERSITÄT BONN
Physikalisches Institut

Monte Carlo Study of the Measurement of the $t\bar{t}$ Production Cross Section in the Muon + Jets Channel with the DØ-Detector at $\sqrt{s} = 1.96$ TeV

von
Jörg Meyer

Abstract: A measurement of the $t\bar{t}$ production cross section at $\sqrt{s} = 1.96$ TeV with the DØ detector using simulated events is performed. The final state containing a muon and jets is examined including all methods of measuring signal efficiencies and the estimation of the background contributions. Especially, the identification efficiency and properties of muons are studied.

Post address:
Nussallee 12
D-53115 Bonn
Germany

BONN-IB-2004-09
Bonn University
März 2004

UNIVERSITÄT BONN
Physikalisches Institut

Monte Carlo Study of the Measurement of the $t\bar{t}$ Production Cross Section in the Muon + Jets Channel with the DØ-Detector at $\sqrt{s} = 1.96$ TeV

von
Jörg Meyer

Dieser Forschungsbericht wurde als Diplomarbeit von der mathematisch - naturwissenschaftlichen Fakultät der Universität Bonn angenommen.

Angenommen am: 1. März 2004
Referent: Prof. Dr. N. Wermes
Korreferent: Prof. Dr. I. Brock

Contents

Contents i

1 Introduction 1

2 Theoretical Basis 3
2.1 The Standard Model of Elementary Particle Physics . . . 3
2.2 Physics of the Top Quark . . . 4
2.2.1 Mass and Lifetime . . . 4
2.2.2 The Top Quark in the Standard Model and Beyond . . . 5
2.2.3 Theoretical Prediction of the Top Quark and Higgs Boson Mass . 5
2.2.4 Production of Top Quarks . . . 6
2.2.5 CKM Matrix Element V_{tb} . . . 9
2.2.6 Decay of Top Quarks . . . 10
2.3 Signal and Background Signature . . . 10
2.3.1 μ + Jets Channel . . . 11
2.3.2 Background . . . 11
2.3.3 τ + Jets Channel . . . 12

3 The Experiment 13
3.1 The Tevatron . . . 13
3.2 The DØ Detector . . . 13
3.2.1 The Inner Tracker System . . . 14
3.2.2 The Calorimeter . . . 16
3.2.3 The Muon System . . . 17
3.2.4 The Trigger System . . . 19
3.3 Monte Carlo Simulations . . . 19
3.3.1 Event Simulation . . . 19
3.3.2 QCD Multi-jet Events . . . 20

4 Object Identification 21
4.1 Jet Studies . . . 21
4.1.1 Jet Energy Scale . . . 22
4.1.2 Jet Identification . . . 23

4.2 Missing Transverse Energy . . . 24
4.3 Muon Studies . . . 24
4.3.1 Muon Reconstruction . . . 24
4.3.2 Quality of Muons . . . 25
4.3.3 Muon Identification Efficiency . . . 25
4.3.4 Distance of Closest Approach . . . 31
4.3.5 Muon Isolation . . . 33

5 Monte Carlo Cross Section 39
5.1 Preselection . . . 39
5.1.1 Muon Identification . . . 39
5.1.2 Muon Tracking . . . 40
5.1.3 Loose Isolation . . . 40
5.1.4 Transverse Muon Momentum . . . 40
5.1.5 Primary Vertex . . . 41
5.1.6 Muon Significance of the Distance of Closest Approach . . . 41
5.1.7 Muon Trigger . . . 42
5.1.8 Jet Identification and Jet Multiplicity . . . 43
5.1.9 Jet Trigger . . . 43
5.1.10 Missing Transverse Energy . . . 45
5.1.11 Summary of all Preselection Cuts . . . 46
5.2 Matrix Method . . . 47
5.3 Berends Scaling . . . 48
5.4 Monte Carlo Study of the Berends Scaling . . . 50
5.4.1 W + jets Monte Carlo Samples . . . 50
5.4.2 Signal Monte Carlo Sample . . . 52
5.4.3 Introducing and Correcting the Trigger Bias . . . 52
5.4.4 Berends Scaling Fit . . . 53
5.5 Topological Analysis of $\sigma(t\bar{t} \to \mu + \text{jets})$ . . . 55
5.5.1 Topological Variables . . . 55
5.5.2 Simulation of the Topological Analysis of $\sigma(t\bar{t} \to \mu + \text{jets})$ . . . 57
5.6 Cross Section Measurement . . . 57

6 Study of Systematic Uncertainties 60
6.1 Background, Efficiency, and Luminosity . . . 60
6.2 Jet Energy Scale . . . 60
6.3 Parton Cuts . . . 63
6.4 Summary of the Systematic Uncertainties . . . 64
6.5 Other Systematic Uncertainties . . . 65

7 Summary and Outlook 67

Bibliography **68**

Acknowledgement **71**

1 Introduction

The aim of elementary particle physics is the understanding of the fundamental constituents of matter and their interactions. Theorists try to explain the various processes in nature with minimal assumptions and fundamental principles. Experimentalists investigate physics at smaller and smaller scales corresponding to higher energies. Particle colliders provide the possibility to study the interaction of particles or the production of new particles. The accelerator facilities and detector systems become very involved and complex, thus there are only a few centers of high energy physics experiments in the world with international collaborations. In the last half century elementary particle physics has made enormous progress. The successful interplay of the theory and experiments has established the so-called Standard Model [1, 2, 3] that sofar describes all observed phenomena of high energy physics.
The heaviest known particle of the Standard Model is the top quark. At present, the hadron collider *Tevatron* at FERMILAB is the only collider in the world that provides enough energy to produce top quarks. It is a great challenge to measure the properties of the top quark with the two experiments CDF and DØ at the *Tevatron*. Top quark physics tests the Standard Model, but is also a search for new physics. Furthermore, the top quark mass is an important parameter of the Standard Model. Its precise knowledge is highly desired to indirectly infer on the mass of the Higgs boson.
This thesis analyzes methods of measuring the top pair production cross section with the DØ detector. The considered final state consists of a muon, a neutrino, and jets. Most quantities that have to be determined to measure the cross section are obtained from data, i.e. the use of simulations is avoided whenever possible. However, the methods can be applied to simulated Monte Carlo events in order to cross-check their validity or precision. One main topic of this thesis are such tests for the muon reconstruction and properties measurements. Moreover, the main analysis parts of the production cross section measurements are performed with simulated events yielding a comparison of the simulated and extracted cross section. Differences between the data analysis and Monte Carlo studies are shown.
The thesis has the following structure:

- Chapter 2 gives a brief overview over the Standard Model and introduces the field of top physics. The signal signature and background processes are discussed.
- Chapter 3 describes the experiment. The characteristics of the *Tevatron* and of

the DØ detector are given.

- In the fourth Chapter the reconstruction and properties of jets, missing transverse energy and muons is explained and studied.
- The measurement of the cross section with simulated events is shown in Chapter 5. It starts with the description of a preselection and illustrates how to separate the signal from different background types. After a final selection the $t\bar{t}$ production cross section and its statistical uncertainty is determined.
- Chapter 6 discusses the systematic uncertainties.
- In the last Chapter 7 the studies are summarized and an outlook on future analyses is given.

2 Theoretical Basis

This chapter gives a brief overview over the theory of elementary particles and their interactions. Especially, the properties and interactions of the top quark, the heaviest known elementary particle, will be presented.

2.1 The Standard Model of Elementary Particle Physics

All known [1] matter in the universe consists of fermions, the leptons and quarks. There are six leptons: the electron, its associated electron neutrino, the muon with its associated muon neutrino, and the tau with its associated tau neutrino. The six quarks are called up, down, charm, strange, top, and bottom. The interactions of elementary particles are well described by the so-called Standard Model [1, 2, 3]. It groups leptons and quarks in three generations:

$$\text{Leptons:} \quad \begin{pmatrix} \nu_e \\ e \end{pmatrix} \quad \begin{pmatrix} \nu_\mu \\ \mu \end{pmatrix} \quad \begin{pmatrix} \nu_\tau \\ \tau \end{pmatrix}$$

$$\text{Quarks:} \quad \begin{pmatrix} u \\ d \end{pmatrix} \quad \begin{pmatrix} c \\ s \end{pmatrix} \quad \begin{pmatrix} t \\ b \end{pmatrix}$$

Particles of the second and third generation have the same quantum numbers as the ones of the first generation, but their masses are larger. In addition, it exists an anti-fermion to every fermion with reversed intrinsic quantum numbers like electric charge.
There are four fundamental interactions: the gravitational, electromagnetic, weak, and strong interaction. Gravity is not described in the Standard Model, but its influence on elementary particles is negligible. The Glashow-Weinberg-Salam theory (GWS) unifies the electromagnetic and weak interaction. Quantumchromodynamics (QCD) is the theory of the strong interaction. Quarks are the only strongly interacting fermions. The GWS model and QCD are quantum field theories that are described by the Standard Model Lagrangian. All interaction terms arise from the requirement of local gauge invariance of the Lagrangian. The gauge symmetries are:

$$\mathrm{SU}(3)_C \times \mathrm{SU}(2)_L \times \mathrm{U}(1)_Y.$$

[1] Cosmology indicates, that the universe consists of about 25% dark matter and 70% dark energy, whose nature is unknown.

interaction	bosons
electroweak	γ, W^+, W^-, Z
strong	8 gluons

Table 2.1: Fundamental interactions and their mediating gauge bosons.

The indices C, L, and Y refer to the color quantum number of quarks, the third isospin component of lefthanded particles, and hypercharge, respectively. The generators of the gauge groups introduce massless gauge bosons that mediate the interactions. $\mathrm{SU}(3)_C$ has eight generators leading to eight gluons that mediate the strong interaction. Explicit fermion mass terms are forbidden in the Lagrangian by the $\mathrm{SU}(2)_L$ symmetry. Therefore, in the GWS theory the gauge invariance of the Lagrangian is spontaneously broken by introducing a Higgs field [4, 5, 6].

$$\mathrm{SU}(2)_L \times \mathrm{U}(1)_Y \rightarrow \mathrm{U}(1)_Q \qquad \mathrm{Q} = \text{electric charge}$$

The result of the so-called Higgs mechanism are massive $W^{\pm}$ and Z boson, whereas the photon γ belonging to the $\mathrm{U}(1)_Q$ remains massless. Moreover, it predicts the existence of a massive scalar Higgs boson, the only elementary particle of the Standard Model, that has not been discovered, yet. Fermion masses are generated by the so-called Yukawa couplings of the Higgs to the fermions.
An introduction to the Standard Model including the historical development can found in [7].

2.2 Physics of the Top Quark

The top quark was discovered at *Fermilab* in 1995 [8, 9]. From 1992 until 1996 the hadron collider *Tevatron* was in the first data taking period, called Run I, and operated at a center of mass energy of $\sqrt{s} = 1.8$ TeV. The two experiments CDF and DØ collected data with an integrated luminosity of $\mathcal{L} \approx 125$ pb^{-1}. In Run I the top quark mass was determined, the top-pair production cross section was measured, and various decay channels were analyzed. However, there are still a lot of interesting measurements to make such as increasing the precision of the top mass, determining the top quark charge, measuring the helicity of the W boson, that originates from a top quark decay, determining the spin correlation of top pairs, or investigating the Yukava coupling of the Higgs boson to the top quark.

2.2.1 Mass and Lifetime

The combined result for the world-average of the top mass was found to be [10]

$$m_t = 174.3 \pm 5.1 \text{ GeV}.$$

Thus, the top quark is by far the heaviest elementary particle. As a consequence of the large mass, the top quark has an extreme short lifetime of

$$\tau_t \approx 0.5 \times 10^{-24} \text{ s}.$$

2.2.2 The Top Quark in the Standard Model and Beyond

The discovery of the top quark completes the three generation Standard Model. However, in order to ensure that the top quark is really the particle with the properties that are predicted by the Standard Model many more measurements have to be performed. Quantum numbers such as spin or isospin or the spin correlation of a top anti-top pair yet have to be tested. So far, only the mass, lifetime, strong production, and the decay modes are known. Due to the high mass and short life time the top quark behaves different from lighter quarks. Top quarks decay before they have time to hadronize, i.e. there are no bound states of top quarks. All other quarks form bound states of mesons or baryons on a time scale given by $\frac{1}{\Lambda_{\text{QCD}}} \approx \frac{1}{200 \text{ MeV}} \approx 3 \cdot 10^{-24}$ s. Therefore the spin information of top quarks are conserved in the decay products. Top physics is a good way to test the Standard Model and the top mass is an important parameter. But the interest in top physics is not only motivated by completing electroweak precision data and testing the Standard Model. The top quark mass is approximately the scale of electroweak symmetry breaking. Hence, it can be speculated that the top quark might play a special role in nature [11]. Its Yukawa coupling to the Higgs field is given by

$$y_t = \sqrt{2}\frac{m_t}{v} \approx 1,$$

where v is the vacuum-expectation value of the Higgs field. The value of y_t might be a hint, that y_t is more fundamental. Maybe, the physics of the top quark leads to the discovery of "new" physics beyond the Standard Model. Another important point of the top quark is the relation to Higgs physics. The Higgs mass can be predicted with the help of the top mass as explained in the next section. Moreover, top production is one of the main backgrounds for many Higgs searches.

2.2.3 Theoretical Prediction of the Top Quark and Higgs Boson Mass

Before the discovery of the top quark its existence was predicted due to the effects of virtual top quarks. The GWS theory allows to calculate the mass of the W boson at tree level taking the electromagnetic coupling α, the Fermi constant G_F, and the Z boson mass M_Z as parameters. These parameters are measured with high precision. However, higher order corrections also contribute to M_W. The one-loop corrections depend quadratically on the top quark mass m_t and logarithmically on the Higgs boson mass M_H [12]. Since the dependency on m_t is much stronger than on M_H, the measurement

of M_W allowed to predict an estimation of the top quark mass m_t. The precision of the prediction increased with a more accurate measurement of the input parameters. It was in full agreement with the discovery. Figure 2.1 [13] shows the χ^2 as function of the top mass of a fit to electroweak precision data. The minimum of the curves refer to the most probable top mass. With the help of the measured top mass m_t the same method is used

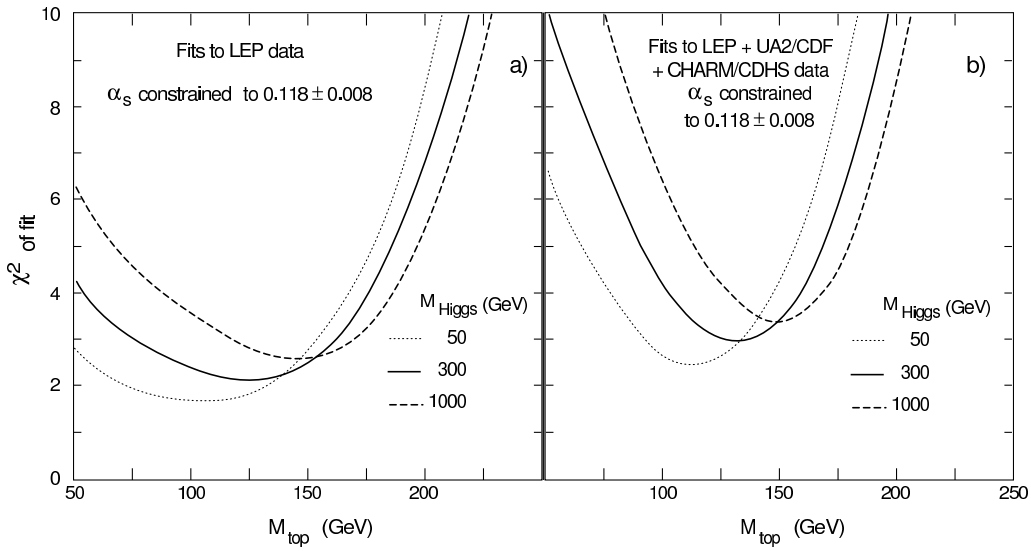

Figure 2.1: χ^2 vs.m_t from a fit to LEP data a) and to LEP, $p\bar{p}$ collider, and ν data b) taken from [13].

to predict the mass of the Higgs boson M_H. In Figure 2.2 taken from [14] M_W is plotted versus m_t. The dashed ellipse shows the direct measurements of M_W and m_t with 68% CL and the solid ellipse shows the indirect 68% CL measurement from fitting precision electroweak data [14]. The plot also shows lines of constant Higgs mass according to the Standard Model.

2.2.4 Production of Top Quarks

At the *Tevatron* top quarks are produced in proton anti-proton collisions. However, not the full center of mass energy of the hadron collider is available for the production of new particles. The hard scattering process is an interaction of quarks or gluons (partons) that are the constituents of the protons and anti-protons. The structure of (anti-) protons is quite complex. They are composites of three valence (anti-) quarks which are bound by gluons. In addition to the valence quarks the (anti-) protons contain many virtual so-called sea quarks. Each parton i inside the (anti-) proton with four-momentum p_i carries only an energy-momentum fraction x_i of p_i. Figure 2.3 (left) sketches the collision of a proton with momentum four-vector p_1 and an anti-proton with momentum four-vector

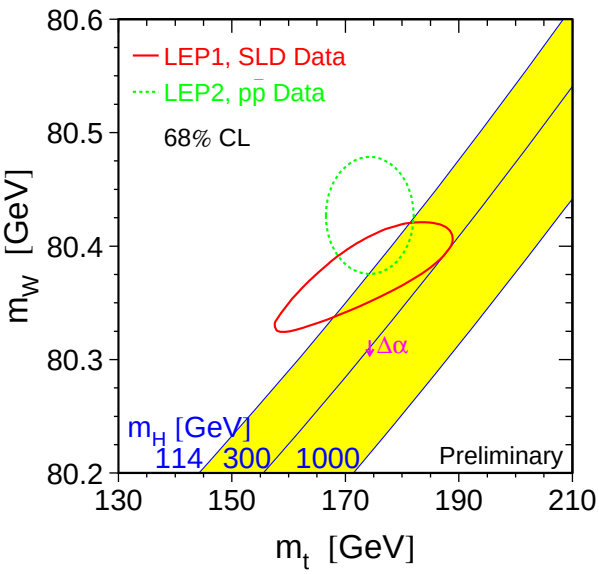

Figure 2.2: M_W vs. m_t with lines of constant Higgs mass and the results of measuring M_W and m_t directly (dashed ellipse) and indirectly (solid ellipse) at 68% CL, [14].

p_2. The squared center of mass energy of the proton anti-proton collision is given by

$$s = (p_1 + p_2)^2 \approx 2p_1 \cdot p_2.$$

However, the squared energy $\hat{s}$ of the partonic subprocess is

$$\hat{s} = (x_1 p_1 + x_2 p_2)^2 \approx 2x_1 x_2 p_1 \cdot p_2 = x_1 x_2 s.$$

The structure of (anti-) protons has been measured in deep elastic scattering experiments. Figure 2.3 (right) gives an example of parameterized parton density functions for each parton type [15]. The function $xf(x, Q^2)$ is the probability-density of finding a parton with momentum fraction x inside the proton, where Q^2 is the inverse of the spatial resolution. Top quarks can be produced via strong or weak interactions.

Strong Production

In Figure 2.4 all tree level Feynman diagrams of the strong top quark production can be seen. They are always produced in $t\bar{t}$ pairs either by quark anti-quark annihilation or gluon fusion. The relative fraction of those subprocesses is determined by the relative amplitudes of the Feynman diagrams and the proton structure function of the

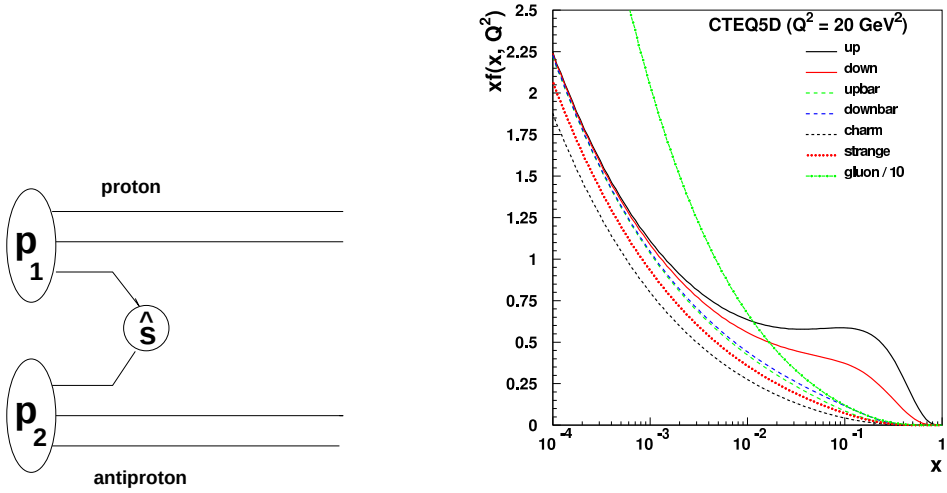

Figure 2.3: Sketch of a parton model of a proton anti-proton collision (left) and the proton structure function from [15] (right). The curve of the gluon is suppressed by a factor of 0.1.

corresponding center of mass energy of the collider. Table 2.2 gives the fractions for the *Tevatron* and for the proton proton collider *Large Hadron Collider* LHC which is presently being built at *CERN* in Geneva. Knowing the top mass, the $t\bar{t}$ production cross section can be calculated in QCD. Measuring the mass and cross section independently makes it possible to compare the directly measured cross section with the calculated cross section, i.e. to test QCD.

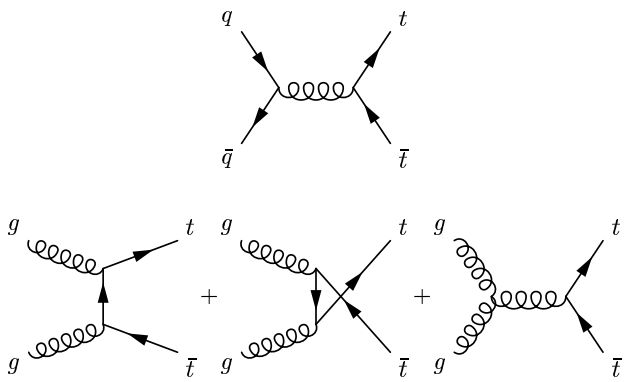

Figure 2.4: Tree level Feynman diagrams for strong $t\bar{t}$ production.

Hadron collider	$\sqrt{s}$	$q\bar{q}$ annihilation	gluon fusion
Tevatron Run I ($p\bar{p}$)	1.8 TeV	90%	10%
Tevatron Run II ($p\bar{p}$)	1.96 TeV	85%	15%
LHC (pp)	14 TeV	10%	90%

Table 2.2: Fraction of $q\bar{q}$ annihilation and gluon fusion for different hadron colliders and energies $\sqrt{s}$.

Weak Production

Beside the $t\bar{t}$ production single top quarks can be produced via the weak interaction. The leading order Feynman diagrams can be seen in Figure 2.5. So far, the single top production has not been observed, but the first observations at *Tevatron* are expected this year. Studying single top production tests the electroweak properties of top quarks.

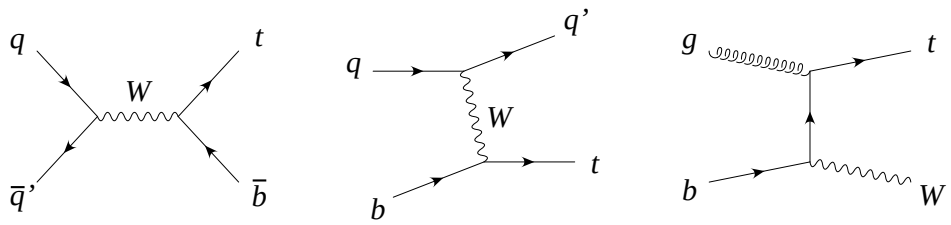

Figure 2.5: Tree level diagrams for weak single top production.

2.2.5 CKM Matrix Element V_{tb}

The physical quark states mix in the weak interaction, i.e. the weak quark eigenstates are obtained by the Cabibbo-Kobayashi-Maskawa (CKM) mixing matrix [16, 17]. A first direct measurement of the CKM matrix element V_{tb} will be possible by analyzing single top events. The CKM matrix has to be unitary. This constraint allows to calculate precisely V_{tb} with the help of other light quark CKM matrix elements that have already been measured [18]:

$$V_{tb} = 0.9990 - 0.9993. \tag{2.1}$$

However, this is only valid for three quark generations. If the direct determination of V_{tb} agreed with Equation 2.1 a further confirmation of the three generation Standard Model would be found. Otherwise, new physics would be found. The direct measurement will not be able to decrease the uncertainty in V_{tb}.

2.2.6 Decay of Top Quarks

Since $V_{tb} \approx 1$ almost 100% of the top quarks decay into a b-quark and a W boson. Therefore, the final state of a $t\bar{t}$ event is determined by the decay modes of the W boson. Figure 2.6 shows all decay channels and there theoretical branching ratios. This thesis discusses the $t\bar{t}$ production in the $t\bar{t}\,(\rightarrow W^+W^-b\bar{b}) \rightarrow \mu\nu b\bar{b}jj'$, the so-called μ + jets channel. The branching ratios of the W-boson are measured to be

$$\mathrm{BR}(W \rightarrow \mu^+\nu) = 10.57 \pm 0.22\%$$

$$\mathrm{BR}(W \rightarrow \mathrm{hadrons}) = 67.96 \pm 0.35\%.$$

Assuming

$$\mathrm{BR}(t \rightarrow Wb) = 100\%$$

the branching ratio of the $t\bar{t} \rightarrow \mu + \mathrm{jets}$ channel yields

$$\mathrm{BR}(t\bar{t} \rightarrow \mu + \mathrm{jets}) = 14.4\%$$

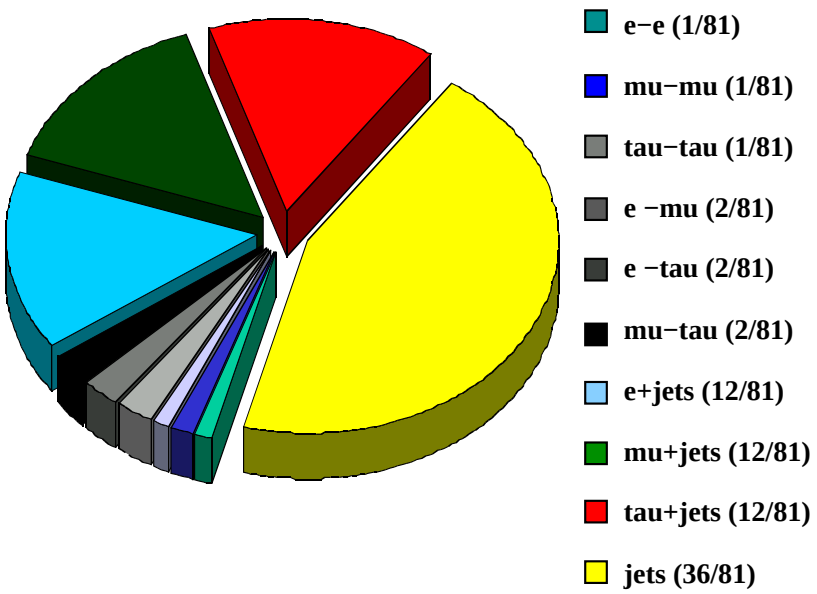

Figure 2.6: All decay channels and approximate branching ratios of $t\bar{t}$ pairs.

2.3 Signal and Background Signature

This section repeats the signature of the $t\bar{t} \rightarrow \mu + \mathrm{jets}$ channel and discusses the main background sources.

2.3.1 μ + Jets Channel

As mentioned in the previous section the final state of a $t\bar{t}$ event is characterized by the decay modes of the W bosons. In the μ + jets channel one W boson decays hadronically, the other one decays into a muon and a neutrino. Moreover, there are four jets, where two of the jets are b-jets, i.e. they arise from b-quarks. Due to the high mass of top quarks and W bosons the jets and leptons tend to be in the central region of the detector and to have a large transverse momentum p_t. Muons from $t\bar{t} \to \mu +$ jets events come from the primary vertex and are isolated from jets, where the exact meaning of isolation will be defined in Section 4.3.5.

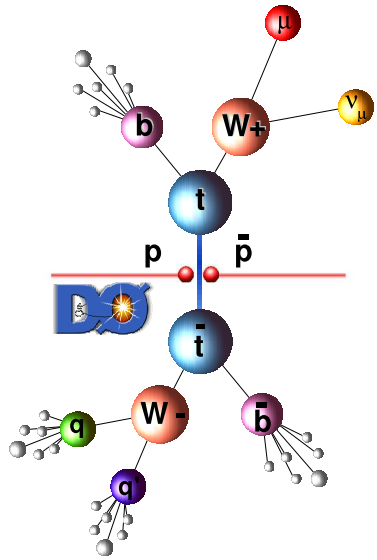

2.3.2 Background

Background events are processes other than $t\bar{t} \to \mu +$ jets that mimic the topology of the $t\bar{t} \to \mu +$ jets signal events. There are two classes of background:

- The first background class consists of QCD multi-jet events containing a muon and faking a neutrino by mismeasured missing transverse energy, $\not{E}_t$ (see Section 4.2). The muon originates from a heavy flavor decay, e.g. from the decay of a B-meson. This means that the muon is inside a jet. Mesons have a long lifetime (τ of B-mesons $\approx 10^{-12}s$) thus their boost allow them to travel several millimeters before they decay at a secondary, displaced vertex. There are preselection cuts to discriminate such muons from signal muons that will be explained in Sections 5.1. One of these variables is the muon isolation, which is a measure of whether a muon is inside a jet or not. Muons of QCD multi-jet events, that pass the preselection are real reconstructed muons, but their isolation is faked. Indeed, the probability for this to happen is rather small, but a lot of events remain due to the high cross section of the strong production of heavy flavor jets.

- The second background class consists of W + jets events with a W boson decaying into a muon and a muon neutrino. This is the main background for $t\bar{t} \to \mu +$ jets events. In contrast to muons from QCD events, muons from W + jets events are not inside of jets and come from the primary vertex as signal muons. The jets are mainly produced by initial and final state radiation or gluon splitting. Figure 2.7 gives examples of Feynman diagrams for W + jets events with different

jet multiplicities. These jets tend to direct in the forward region to have a small transverse energy. But W + jets events with high E_t central jets are more difficult to distinguish from signal events. To estimate the number of W + jets events passing the preselection the Berends scaling [19] method described in Section 5.3 will be applied.

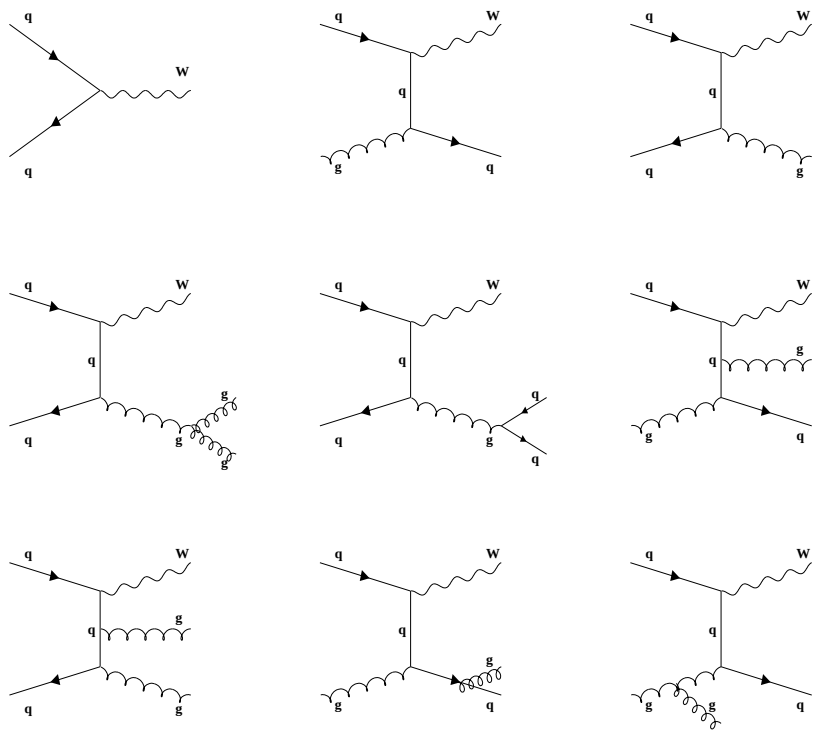

Figure 2.7: Examples of Feynman diagrams for W + jets events with different jet multiplicities.

2.3.3 τ + Jets Channel

The $t\bar{t} \to \tau$+jets channel is equivalent to the $t\bar{t} \to \mu$+jets channel with a tau instead of a muon. If the tau decays to a muon ($\tau^- \to \mu^- \bar{\nu}_\mu \nu_\tau$ and charge conjugated), the final state will be similar to the $t\bar{t} \to \mu +$jets final state. Hence, those events have to be included in a μ + jets data analysis. The branching ratio has to be adapted correspondingly and the Monte Carlo samples to measure efficiencies have to include $t\bar{t} \to \tau(\to \mu\nu\nu) +$jets events, as well. The Monte Carlo studies done in this thesis are however carried out without considering $t\bar{t} \to \tau +$jets events.

3 The Experiment

This chapter introduces the DØ experiment. First, the main characteristics of the *Tevatron* are given. Thereafter the main DØ subdetector systems which are important to measure muons and jets are described. These are the inner tracking system, the calorimeter, and the muon system. In addition, a brief overview of the trigger system is given. Finally, the steps to produce Monte Carlo events are explained.

3.1 The Tevatron

The *Tevatron* is a proton anti-proton accelerator and collider at FERMILAB located near Chicago. At present the *Tevatron* is the highest-energy collider in the world with a center-of-mass energy of 1.96 TeV. There are two detectors at the *Tevatron*: CDF and DØ. A first data taking period from 1992 until 1996 is called Run I. The center-of-mass energy in Run I was 1.8 TeV. Both experiments collected about 125 pb^{-1} of data. After Run I, the accelerator and both detectors were upgraded. Besides the higher center-of-mass energy the luminosity was increased to be $8.6 \cdot 10^{31}$ $\mathrm{cm}^{-2}\mathrm{s}^{-1}$ (design value). The proton and anti-proton beam has a bunch structure with 36 bunches in each beam and a bunch crossing time between crossings of 396 ns. The data taking of Run II started in March 2001. In spring 2004 there will be about 210 pb^{-1} data analyzed by the DØ collaboration. The *Tevatron* is expected to deliver 4 fb^{-1} to 9 fb^{-1} until the end of Run II in 2009. For details of the *Tevatron* in Run II, see [20].

3.2 The DØ Detector

The coordinate system to specify a position or direction in the detector is explained. The proton beam runs in the positive z-direction. Positions in the transverse xy-plane are given by r and ϕ, where

$$r = \sqrt{x^2 + y^2} \qquad \phi = \tan \frac{y}{x}, \quad \phi \in [0, 2\pi].$$

To denote the polar angle θ the pseudo-rapidity η is rather used than θ, because differences of rapidities are Lorentz invariant. The pseudo-rapidity η is defined as

$$\eta = -\ln \tan \frac{\theta}{2}.$$

In Figure 3.1 the cross section of the DØ detector can be seen and Figure 3.2 shows a quarter of the inner tracking system. A detailed description of the upgrade of the DØ detector after Run I can be found in [21, 22].

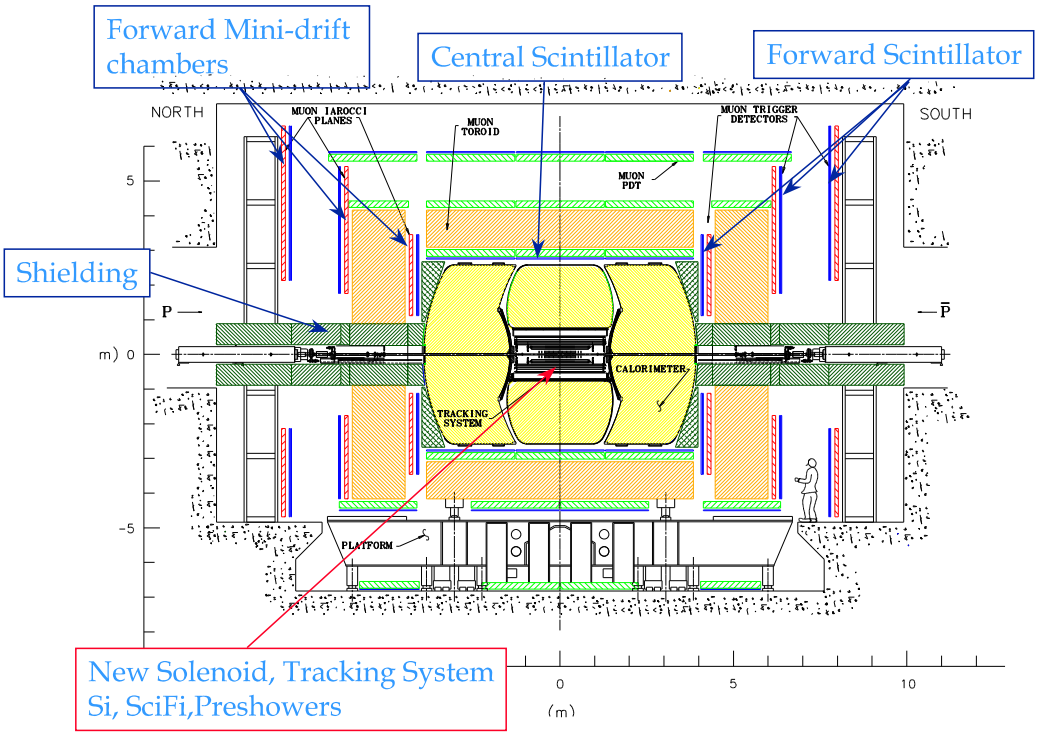

Figure 3.1: Cross-sectional view of the DØ detector.

3.2.1 The Inner Tracker System

The tracking system consists of the Silicon Microstrip Tracker (SMT) and the Central Fiber Tracker (CFT). Figure 3.3 shows the SMT. It is the innermost subdetector of the DØ experiment. To reconstruct tracks in the central region there are six barrels and in the forward region there are twelve so-called F-disks and four H-disks. They allow tracking in a range up to $|\eta| < 3.0$. A particle traversing a barrel hits at least four layers of silicon detectors. The SMT has 793,000 readout channels.

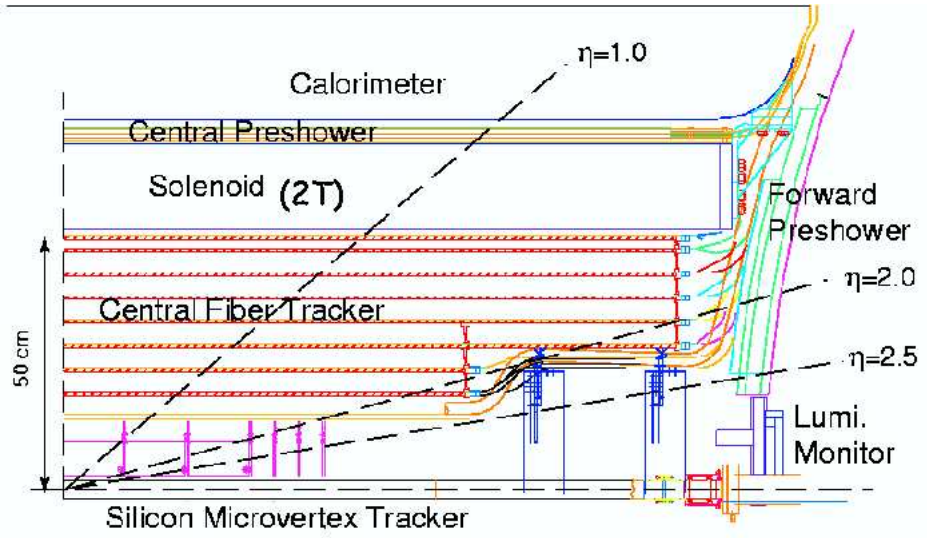

Figure 3.2: Quarter of the inner tracking system.

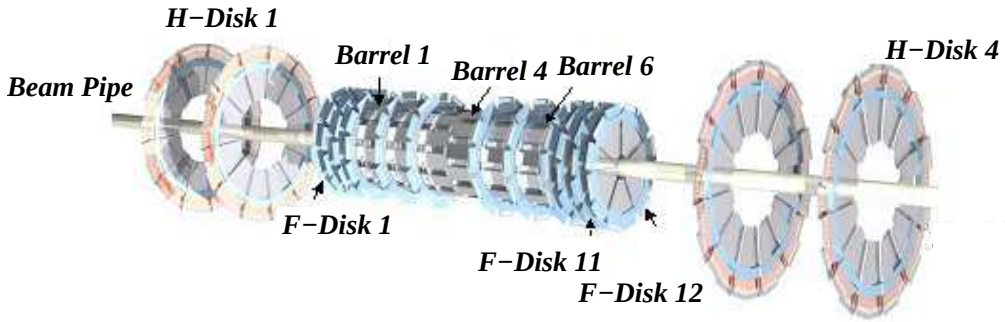

Figure 3.3: Silicon Microstrip Detector consisting of six barrels, twelve F-disks, and four H-disks.

Around the SMT there is the CFT as can be seen in Figure 3.2. Eight cylindric layers of scintillating fibers make tracking in the range $|\eta| < 1.62$ and fast Level 1 triggering possible. The maximum η for CFT hit is $|\eta| < 2.0$. Altogether there are about 74,000 fibers. The fibers produce yellow-green light ($\lambda \approx 530$ nm) that is conducted by waveguides to photodetectors. These are SiAs avalanche photodiodes, so-called Visible Light Photon Counters (VLPC). The VLPC are inside a liquid helium cryostat at a temperature of 9.00 ± 0.05 K to operate at a noise rate of less then 0.1%. Stereo angles in the SMT and CFT allow a three dimensional reconstruction of particle tracks. The CFT has an outer radius of about 60 cm. The whole tracking system is surrounded by a superconducting solenoid magnet that provides a 2 T magnetic field. With the help

of the tracking system primary vertices and displaced secondary vertices can be found. Due to the solenoidal field a high precision measurement of the transverse momentum p_t of charged particles is possible.

3.2.2 The Calorimeter

The calorimeter measures the energy of photons, electrons, and jets. It is divided in three parts: the central calorimeter and two end calorimeters as shown in Figure 3.4. The electromagnetic calorimeter consists of the inner layers of the central and the end calorimeters. The outer layers are called fine hadronic and coarse hadronic calorimeter corresponding to the granularity. The DØ-calorimeter is a liquid argon sampling calorimeter with uranium absorber material. It is a compensating calorimeter, i.e. the ratio of the electromagnetic and hadronic response is $e/h \approx 1$. In the coarse hadronic section (see Figure 3.4) copper and steel is used as absorber. In Figure 3.5 the hermetic coverage up to $|\eta| < 4.2$ can be seen. A calorimeter cell is a unit of absorber and active detector. The calorimeter cells are arranged in projective towers. A characteristic of

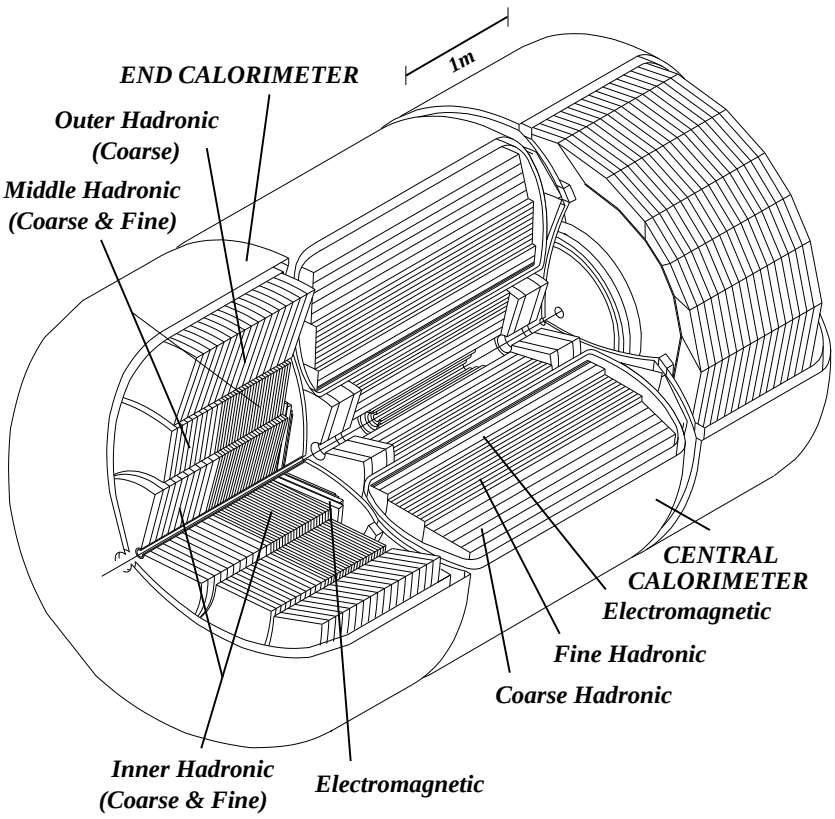

Figure 3.4: Central and End Calorimeters.

the DØ calorimeter is the fine granularity. The transverse segmentation of the readout is typically $\Delta\eta \times \Delta\phi = 0.1 \times 0.1$ and at the shower maximum for electrons even 0.05×0.05. The energy resolution of the electromagnetic and hadronic calorimeter are measured with an electron and pion beam, respectively [23]. The result for the resolution of the electromagnetic calorimeter is:

$$\frac{\sigma_E}{E} = \sqrt{0.014^2 + \frac{(0.135\sqrt{\text{GeV}})^2}{E} + \frac{(0.14\ \text{GeV})^2}{E^2}},$$

and for the hadronic calorimeter (in the end calorimeter, middle hadronic section):

$$\frac{\sigma_E}{E} = \sqrt{0.032^2 + \frac{(0.41\sqrt{\text{GeV}})^2}{E} + \frac{(1.3\ \text{GeV})^2}{E^2}}.$$

The statistical fluctuations of a calorimeter are proportional to $E^{-1/2}$. The constant term parameterizes calibration errors and the term proportional to E^{-1} takes noise contributions into account.
Altogether, there are about 55,000 readout channels for the calorimeter.

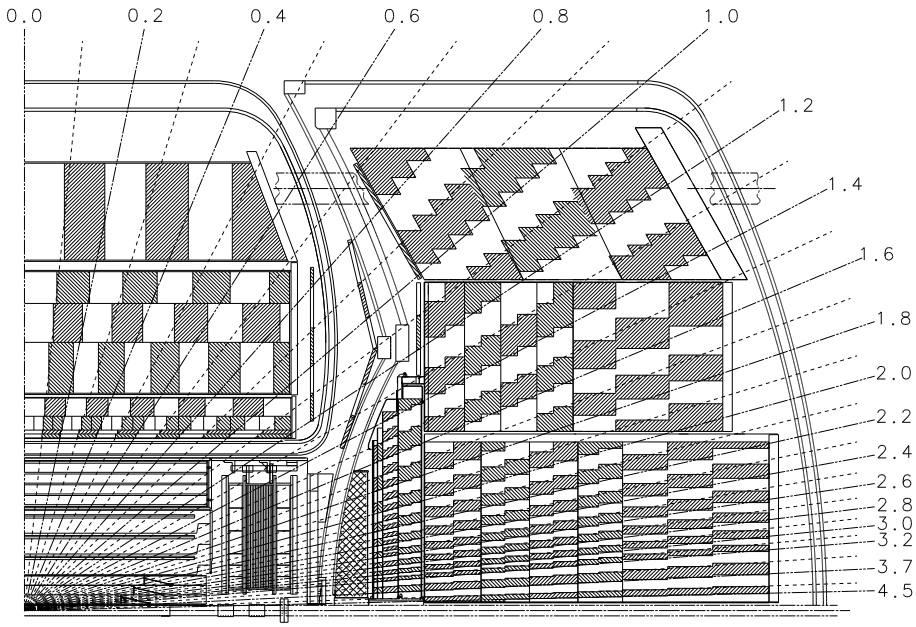

Figure 3.5: View of a quarter of the calorimeter. The projective towers and $\Delta\eta$ segmentation can be seen.

3.2.3 The Muon System

The local muon system is the outermost laying subdetector system. It consists of three layers A, B, and C. Each layer consists of drift tubes and scintillation counters.

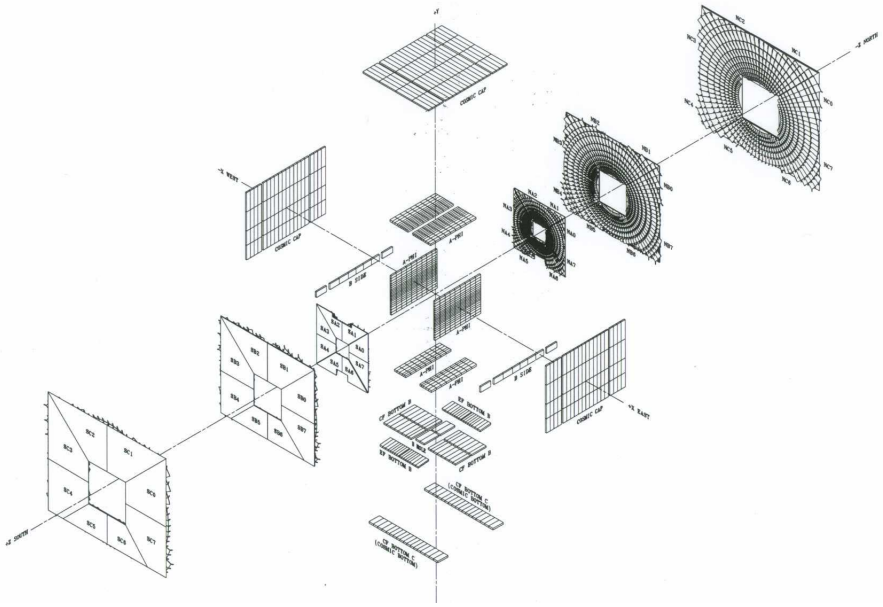

Figure 3.6: Exploded view of the three scintillator layers of the local muon system.

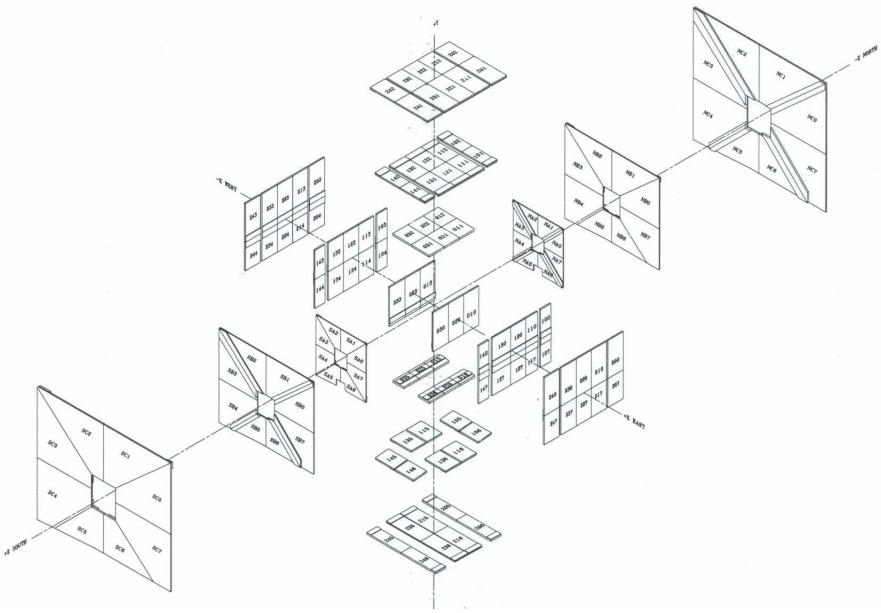

Figure 3.7: Exploded view of the three drift chamber layers of the local muon system.

In the central region ($|\eta| < 1.0$) there are Proportional Dri ft Tubes (PDT), that were already used in Run I. The PDTs consist of 6624 dri ft cells with a size of 10.1×5.5 cm^2. The drift tubes in the forward region ($1.0 < |\eta| < 2.0$) were added for Run II. Because of their smaller geometry they are called Mini Drift Tubes, (MDT). There are 6080 MDTs each with 8 cells with a size of 9.4×9.4 mm^2. Figure 3.6 and 3.7 show exploded views of the scintillation counters and drift tubes. In the bottom region there are acceptance gaps due to the mounting of the detector. The fast signal of the scintillation counters is used by the Level 1 trigger. There are 630 counters in the central and 4214 counters in the forward muon system. Between the inner-most layer A and layer B there is a toroid with a 2 T magnetic field. Therefore the muon system provides a stand-alone measurement of muon momenta.

3.2.4 The Trigger System

There are 2.5×10^6 bunch crossings per second at the *Tevatron*. The task of the DØ-trigger system is to decide which events are stored, because the recording rate is limited to 50 events per second. This is done in three stages, called Level 1, Level 2, and Level 3. The Level 1 trigger is the fastest, but uses only basic information on physics objects with a low resolution. Level 2 decides with more detailed information. The Level 3 trigger consists of farm nodes that make the final decision weather an events is recorded. Table 3.1 gives the rates and decision times for all three stages.

stage	accept rate	decision time
Level 1	2 kHz	$4.2\,\mu s$
Level 2	1 kHz	$\leqslant 100\,\mu s$
Level 3	50 Hz	$\sim$ 50 ms

Table 3.1: Rates and decision times of the trigger stages.

3.3 Monte Carlo Simulations

3.3.1 Event Simulation

Monte Carlo events are simulated in several steps. First, an event generator creates events without simulating the detector. The kinematics of a certain physics process is calculated according to the theory. The event generators used for this thesis calculate only leading order Feynman diagrams. Initial and final state radiation are not calculated with Feynman diagrams, because with increasing number of radiated photons or gluons the calculations become difficult or impossible. Instead of that, empirical parton shower

models are applied. They rely on given probabilities for particles to radiate photons or gluons with a certain momentum. The parton showering simulates all radiated particles at once, thus not every single process has to be considered. Quarks and gluons are not observable final states, but hadrons that are bound states of quarks. The hadronization cannot be described by QCD, because at low energies the strong coupling constant α_s becomes large, thus perturbative calculations are impossible. Therefore, the hadronization is simulated by fragmentation models. This thesis uses *ALPGEN* [24] and *PYTHIA* [25] for the event generation. In both cases the parton showering and fragmentation is done by *PYTHIA*, that includes the program *JETSET* [26]. This program uses the so-called string-fragmentation model described in [26, 25]. After generating events the response of the detector is simulated. The simulation of the DØ subdetector components are based on *GEANT* [27]. Simulated events with full detector simulation are reconstructed the same way as data events. Since the reconstruction software improves continuously there are different software releases. In this thesis either the p13 or the p14 reconstruction release is used.

3.3.2 QCD Multi-jet Events

The correct simulation of jets is difficult. It depends on the used fragmentation model. In addition the simulation of the calorimeter response, noise, and actual performance is never perfect. Therefore, all quantities involving jets are measured with data events as far as possible. However, in this thesis simulated QCD events are used to test methods that are usually applied to data. The QCD multi-jet background described in Section 2.3.2 contains a muon coming from a semi-leptonic decay. There is another problem with the simulation of this type of events. The probability, that a QCD multi-jet contains a high p_t muon is rather small, thus millions of events have to be generated to yield only a small sample with a muon. The muon studies described in Section 4.3.4 and 4.3.5 are performed with a p13 sample that was generated with a muon generator cut of $p_t^\mu > 12$ GeV. But only 16,480 events of them contain a muon with $p_t > 15$ GeV and a match to a central track. To study the matrix method which will be introduced in Section 5.2 a larger sample would be necessary, because the sample would be divided in sub-samples with different jet multiplicities. Most events of the available sample contain only one jet. Unfortunately, it is not possible to generate a sample of appropriate size.

4 Object Identification

The final state of the process discussed in this thesis consists of muons, jets, and missing transverse energy. Hence, this chapter concentrates on the definitions and reconstruction of these physics objects. First, the definition of jets is given. It is explained how the energy measurement is calibrated and how the jet identification efficiency is determined. The calculation of missing transverse energy is described. The main part of this chapter deals with muon studies. After introducing the reconstruction and quality criteria of muons, a method to determine the muon identification efficiency from a data sample is investigated with simulated events. Further muon studies are performed to investigate properties of muons such as "distance of closest approach" and isolation.

4.1 Jet Studies

Jets are reconstructed with the measurement of energy in the calorimeter. The energy of calorimeter cells is clustered with a cone algorithm [28], where the cone size of a jet in η and ϕ is defined to be $R = \sqrt{\Delta\eta^2 + \Delta\phi^2} = 0.5$. The clusters of the cone algorithm have to fulfill several criteria to be reconstructed as jets:

- First of all jets have to be distinguished from photons and electrons. In order to do this a cut on the energy fraction in the electromagnetic calorimeter, EMF, is applied:
$$0.05 < \text{EMF} < 0.95$$
- CHF is the energy fraction that is deposited in the coarse hadronic section, the outermost part of the hadronic calorimeter. Clusters with large CHF are mainly caused by calorimeter noise. To remove such jets, reconstructed jets are required to fulfill:
$$\text{CHF} < 0.4.$$
- Single calorimeter cells with energy depositions that are not related to events are called "hot cells". Energy clusters dominated by hot cells are removed by cutting on the ratio of the transverse energy of the two leading cells in the cluster:
$$\frac{E_t(\text{leading cell})}{E_t(\text{next-to-leading cell})} \equiv \text{HotF} < 10$$

- Calorimeter towers are the combination of calorimeter cells with approximately the same η and ϕ. Hot towers consist of hot cells. To remove them 90% of the jet energy is not allowed be deposit in a single tower:

$$\text{number of towers containing 90\% of the jet energy} \equiv \text{n90} > 1$$

- The ratio of n90 and the number of towers of a jet is called f90. Jets, that mainly contain noise tend to have a large f90. However, jets with small CHF are considered as good jets. To further remove "noise" jets without large inefficiency the following jet identification criteria is required depending on the transverse jet energy:

$$\text{jet } E_t < 25 \text{ GeV: f90} < 0.7 - 0.5 \times \text{CHF or CHF} < 0.025$$

$$\text{jet } E_t > 25 \text{ GeV: f90} < 0.8 - 0.5 \times \text{CHF or CHF} < 0.05$$

4.1.1 Jet Energy Scale

The energy measured in a cone in the calorimeter, E_{measured}, is not the energy of the original parton. To obtain the parton energy, $E_{\text{corrected}}$, a jet energy scale correction has to be applied:

$$E_{\text{corrected}} = \frac{E_{\text{measured}} - O}{R \times S},$$

where O is an energy offset, R is the hadronic calorimeter response, and S is a correction due to the shower energy fraction outside of the jet cone. By subtracting the offset, the jet energy that does not belong to the hard interaction is removed. This energy might come from a soft underlying event, detector pile-up, multiple proton interactions, electronic noise, or uranium "noise". An underlying event is an interaction of spectator partons that are not involved in the hard scattering process, or additional hard interactions. Pile-up energy is residual energy from previous bunch crossing. The number of multiple proton interactions and pile-up depend on the luminosity. Uranium "noise" is caused by radiation from uranium decay. The calorimeter response R is typically smaller than one, which means that not the total energy of a jet is measured, because of losses in regions without detector and the differences in electromagnetic and hadronic particle interactions. All contributions to the jet energy scale correction are determined with data events. For example the hadronic calorimeter response is determined using γ+jet events. The idea is to calibrate the jet energy scale with the help of the photon energy that is measured with the electromagnetic calorimeter. Figure 4.1 sketches such an event. The electromagnetic response of the electromagnetic calorimeter is calibrated using Z, J/Ψ and π^0 data. Due to momentum conservation in the transverse plane the photon γ should balance the E_t of the jet. However, the imperfect calorimeter response causes an imbalance that can be measured to determine R.
The jet energy scale in simulated events is not the same as for data, because of differences

in the simulation of e.g. noise or the calorimeter response. It is measured with the same method as the data jet energy scale. Hence, both jet energy scales have a statistical and systematic uncertainty.

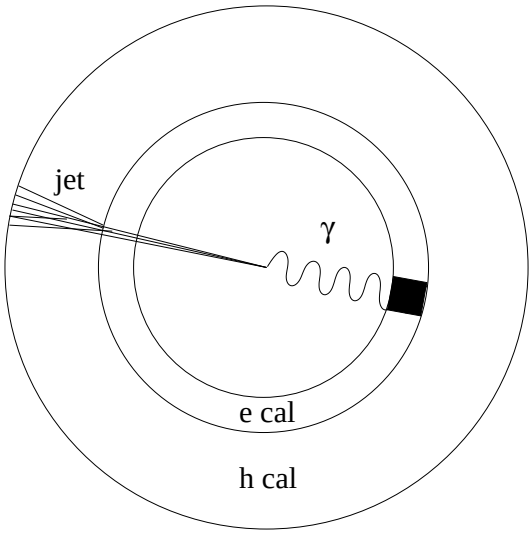

Figure 4.1: Sketch of a γ + jet event. The photon γ deposits energy in the electromagnetic calorimeter (e cal) and the jet in the hadron calorimeter (h cal). Photon and jet energies are balanced, thus the vectorial sum in the plane transverse to the beam vanishes.

4.1.2 Jet Identification

The efficiency to identify jets can be measured using data. One possible method is to use γ + jet events. A reference sample is defined with a high E_t photon and a high E_t calorimeter cluster that is back-to-back to the photon. The cluster is required to be matched to a Level 2 jet and the events are required to have small missing transverse energy, that is defined in the next section. The reference sample contains γ + jet events, where the high E_t photon balances the high E_t jet as sketched in Figure 4.1. The jet identification efficiency is the ratio of events with a reconstructed jet and the total number of events in the reference sample. A detailed description and results of this method can be found in [29].
An alternative method uses di-jet events. Again a reference sample is defined. It contains a well reconstructed jet used as "tag"-jet and back-to-back to the tag-jet a so-called "track"-jet. A track-jet consists of at least two tracks in the inner tracking system that have a small distance. See [30] for a description of the track-jet algorithm. The track-jet is used as probe, i.e. the jet identification efficiency is the number of events where the track-jet is also reconstructed as jet in the calorimeter divided by all events in the

reference sample.
It is important to measure the efficiency for jet-identification using real data in order to be independent of simulations. The simulation of jets and the calorimeter measurement are not accurate enough.

4.2 Missing Transverse Energy

The sum of the transverse energy of all particles in an event vanishes due to energy and momentum conservation. Since neutrinos cannot be detected directly, they cause an imbalance in the vectorial sum of E_t of all detected particles. The energy which is not detected and is missing in the balance is called missing transverse energy, $\not{E}_t$. This makes an indirect measurement of a neutrino possible. All energy deposits in calorimeter cells are taken into account, not only energy of jets. The missing energy measured with calorimeter cells is called "calorimeter missing energy". There are several corrections to $\not{E}_t$. The jet energy scale corrections lead to corrections of $\not{E}_t$. Similarly to the jet energy scale correction there is a so-called em-scale correction for electromagnetic objects also leading to corrections of $\not{E}_t$. The p_t of muons as measured in the central tracker are included in the sum and the energy depositions of high p_t muons in the calorimeter ($\approx$ 3 GeV) are subtracted. In the analysis the $\not{E}_t$ including all above corrections is used. Neutrinos are not the only source of $\not{E}_t$. Energy clusters that are not reconstructed as belonging to jets cannot be jet energy scale corrected, thus they lead to $\not{E}_t$. Another unphysical source of $\not{E}_t$ is calorimeter noise.

4.3 Muon Studies

Muons play an important role in triggering interesting events, and to distinguish different processes and decay channels. They are quite easy to separate from other particles, because muons are the only particles, that can traverse the whole detector material and reach the outermost layer, the muon system. Therefore, the muon system should have a large geometrical acceptance, i.e. it should cover a large angular range in η and ϕ. The DØ muon system fulfills this requirement. It is described in Section 3.2.3. Within the acceptance it is essential to reconstruct muons with a high efficiency.

4.3.1 Muon Reconstruction

Drift chamber and scintillator hits in the local muon system are used to fit local muon tracks. The tracks are bent by the toroidal magnetic field. Therefore, they provide a measurement of the muon momentum p^{local}. Local tracks are extrapolated to the inner tracking system. All central tracks around an extrapolated local track are used to perform a global fit. The track with the best fit is taken as global muon track, which provides a much more precise measurement of the muon momentum.

4.3.2 Quality of Muons

Several hits in drift tubes (w-hits) and scintillation counters (s-hits) are necessary to ensure the detection of a muon. Table 4.1 gives definitions for muons of different reconstruction quality. The loose, medium, and tight definitions are certified in p13, meaning the agreed set of selection criteria of the p13 event software reconstruction version. Positive values of χ^2_{loc} refer to a successfully found track in the local muon system alone. The studies in this thesis only use medium muons for the following reasons. Hadrons which punch through the calorimeter might cause hits in the A-layers, but they are not able to cross the toroid between layer A and B (see Section 3.2.3 for a description of the local muon system). Hence, they are very unlikely to fake a medium muon. With the help of the scintillator hits, muons from cosmic radiation can be identified. The online time resolution of the scintillation counters is ≈ 5 ns and with offline corrections even 2.5 ns. Therefore the time difference Δt between the record of the A-layer hits and the BC-layer hits can be measured. The cut $\Delta t > -10$ ns vetos cosmic muons coming from outside of the detector.

muon type	w-hits A	w-hits BC	s-hits A	s-hits BC	χ^2_{loc}
loose	> 1	> 1	> 0		
loose	> 1		> 0	> 0	
loose		> 1		> 0	
medium	> 1	> 1	> 0	> 0	
tight	> 1	> 2	> 0	> 0	> 0

Table 4.1: The muon quality definitions for loose, medium, and tight muons using the p13 reconstruction code. A muon is called loose, if one of the three definitions is satisfied.

4.3.3 Muon Identification Efficiency

The probability to reconstruct a medium muon within the geometrical acceptance of the local muon system is called muon identification efficiency:

$$\varepsilon^{\mu}_{\text{ID}} = \frac{\text{number of reconstructed medium muons}}{\text{number of all muons within the geometrical acceptance}}. \tag{4.1}$$

A muon is required to satisfy $|\eta| < 2$ and $\phi < 3.9$ or $\phi > 5.5$ for $|\eta| < 1.3$. Thereby, the bottom muon system acceptance gap is cut away very conservatively.
The muon identification efficiency, $\varepsilon^{\mu}_{\text{ID}}$, can be measured with $Z \to \mu\mu$ data events. The advantage of a data method is to be completely independent of simulations. In order to

study this data method it is applied to Monte Carlo events. Making use of the Monte Carlo information allows to determine $\varepsilon^{\mu}_{\mathrm{ID}}$ also with a Monte Carlo method. Comparing the results cross checks the data method with respect to possible systematic effects. Both methods are introduced below.

Monte Carlo Method

In Monte Carlo events the number and properties of all generated muons are known. The number of generated muons in the detector acceptance, and the number of reconstructed medium muons can be looked up and directly plugged into Equation 4.1. However, the Monte Carlo method can only be applied to simulated events.

Data Method

The data method can be applied to measured data events as well as to Monte Carlo events, because there will be no use of quantities, that are only known in the simulation. This means, that the total number of muons in an event is a priori not known. A criterion ensuring that a muon traverses the local muon system, but independent of the local muon system is requested. Figure 4.2 sketches the idea of the data method with $Z \to \mu\mu$ events. Due to the high mass of Z bosons they are produced with a small boost. Hence, the muons of a $Z \to \mu\mu$ event fly almost back-to-back, i.e. $\Delta\phi \approx \pi$.

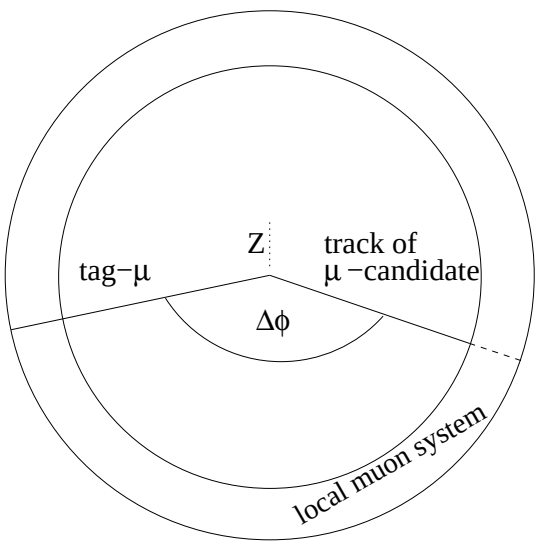

Figure 4.2: Measurement of the muon identification efficiency with $Z \to \mu\mu$ events.

A reference sample is defined by the following cuts and requirements:

- the event contains at least one reconstructed medium muon (tag-muon) with

  - a matched central track
  - a muon $p_t > 15$ GeV
  - isolation (definition and details in Section 4.3.5)
  - a match to a triggered Level 2 muon (in data)

- and event contains a track (muon candidate) with
  - $\Delta\phi(\mu, \text{track}) > 2.5$ (back-to-back requirement)
  - a track $p_t > 15$ GeV
  - track and tag-muon have unlike signed electric charge
  - within the geometrical acceptance of the local muon system

The tag-muon should be clearly identified and tag the event. Its isolation requirement suppresses background events. The meaning of "isolation" will be defined in Section 4.3.5. To discriminate $Z \to \mu\mu$ events from background events the invariant mass of the tag-muon track and the muon candidate track is calculated. The muon identification efficiency measurement is performed only with events where the invariant mass is within the mass window

$$76 \text{ GeV} < \text{invariant mass(tag-}\mu\text{, track)} < 104 \text{ GeV},$$

i.e. around the Z-mass, $M_Z = 91.2$ GeV. Otherwise, the event might not be a $Z \to \mu\mu$ event and the muon candidate track does not belong to a muon. Figures 4.3 show the invariant mass distribution for events with two muons that are identified in the local muon system and the distribution of all events in the reference sample. The Monte Carlo study is performed only with simulated $Z \to \mu\mu$ events. But in the data plot in Figure 4.3 (right) [29] it can be seen that the data reference sample contains lots of background events also in the mass window. However, the number of $Z \to \mu\mu$ events can be determined by a fit to the invariant mass spectrum. The fit function is the sum of an exponentially decreasing function that describes the background distribution, and a Gaussian that approximates the Z-peak. With the help of the fit results the background can be subtracted from the spectra with one or two reconstructed muons. The muon identification efficiency is obtained by dividing the background subtracted number of events with two reconstructed muons by the total background subtracted number of events in the reference sample within the mass window.

Event Weighting

$\varepsilon^{\mu}_{\text{ID}}$ is a function of p_t , ϕ, and η. The MDTs in the forward region are newer than the PDTs in the central region. They also differ in geometry.

Muons from $Z \to \mu\mu$ events and $t\bar{t} \to \mu + \text{jets}$ events have different p_t spectra and

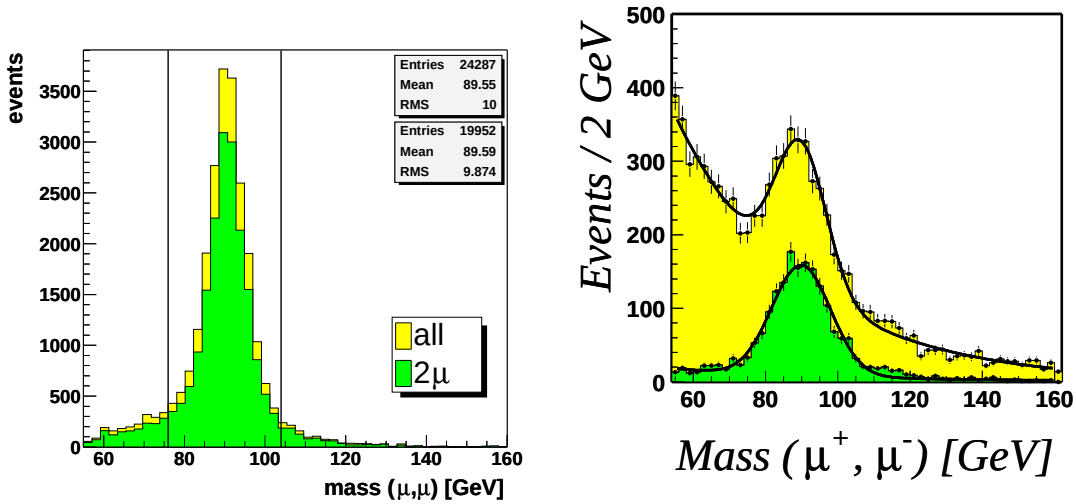

Figure 4.3: Invariant mass of tag-muon track and muon candidate track for all events in reference sample (light grey) and for events, where the candidate is matched to a muon (dark grey), determined with (p13) $Z \to \mu\mu$ Monte Carlo without background (left) and data [29] (right).

different η-distributions, as shown in Figure 4.4. Therefore, the integral over those distributions yields different $\varepsilon^{\mu}_{\mathrm{ID}}$, i.e.

$$\varepsilon^{\mu}_{\mathrm{ID}}(t\bar{t} \to \mu + \mathrm{jets}) \neq \varepsilon^{\mu}_{\mathrm{ID}}(Z \to \mu\mu).$$

Nevertheless, $\varepsilon^{\mu}_{\mathrm{ID}}(t\bar{t} \to \mu + \text{jets})$ can be estimated using $Z \to \mu\mu$ events. The only difference between muons, within a certain small p_t bin, coming from $t\bar{t} \to \mu$+jets events and coming from $Z \to \mu\mu$ event is their η-distributions. This can be taken into account by reweighting each $Z \to \mu\mu$ events in such a way, that the shape of the $Z \to \mu\mu$ η-distribution matches the shape of the $t\bar{t} \to \mu$+jets η-distribution. The weighting factor, $w(\eta\text{-bin}, p_t\text{-bin})$, for a muon within a certain p_t -bin depending on the muon η-bin is the ratio

$$w(\eta\text{-bin}, p_t\text{-bin}) = \frac{\text{no. of generated muons within } p_t\text{- and } \eta\text{-bin in } t\bar{t} \to \mu + \text{jets event}}{\text{no. of generated muons within } p_t\text{- and } \eta\text{-bin in } Z \to \mu\mu \text{ event}}. \tag{4.2}$$

Combining Equation 4.1 and 4.2 one obtains

$$\varepsilon^{\mathrm{ID}}_{\mu}(p_t)(t\bar{t} \to \mu + \text{ jets}) = \frac{\sum_{i \in \{\eta\text{-bins}\}} \text{reconstructed muons } (p_t)(Z \to \mu\mu) \cdot w(i, p_t)}{\sum_{i \in \{\eta\text{-bins}\}} \text{generated muons } (p_t)(Z \to \mu\mu) \cdot w(i, p_t)} \tag{4.3}$$

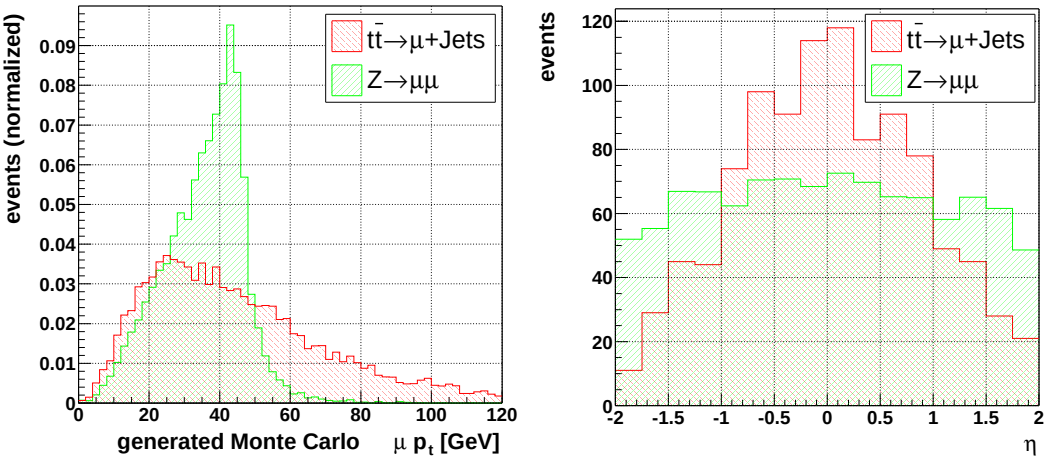

Figure 4.4: Muon p_t spectrum for $t\bar{t} \to \mu +$ jets and $Z \to \mu\mu$ events (left) and muon η-distributions in one p_t -bin: 45 GeV $< p_t <$ 50 GeV (right).

for events within a fixed p_t -bin. Finally, summing over the p_t -distribution yields:

$$\varepsilon_{\mu}^{\mathrm{ID}}(t\bar{t} \to \mu + \text{ jets}) = \frac{\sum_{j \in \{p_t\text{-bins}\}} \sum_{i \in \{\eta\text{-bins}\}} \text{reconstructed muons } (j)(Z \to \mu\mu) \cdot w(i,j)}{\sum_{j \in \{p_t\text{-bins}\}} \sum_{i \in \{\eta\text{-bins}\}} \text{generated muons } (j)(Z \to \mu\mu) \cdot w(i,j)} \tag{4.4}$$

The muon η-distributions have to be taken from the simulated events, because $t\bar{t} \to \mu +$ jets data distributions have insufficient statistics and contain only muons that are already reconstructed.

Comparison of the Results

The Monte Carlo and data method are applied to simulated $Z \to \mu\mu$ events. To obtain $\varepsilon_{\mathrm{ID}}^{\mu}$ for $t\bar{t} \to \mu+$jets events the muon η-weighting that is described in the previous section is used. In addition the Monte Carlo method is directly applied to $t\bar{t} \to \mu +$jets events. Since the proportional drift tubes in the central region ($|\eta| < 1.0$) and the mini drift tubes in the forward region ($1.0 < |\eta| < 2.0$) differ in their geometry the measurements of $\varepsilon_{\mathrm{ID}}^{\mu}$ are done separately for both regions. Figure 4.5 shows the muon identification efficiency versus muon p_t in the central (left) and forward region (right). It can be seen that the efficiency of the newer mini drift tubes in the forward muon system is higher than the efficiency of the proportional drift tubes in the central muon system, that were already used in Run I. Table 4.2 gives the efficiencies integrated over all $p_t > 15$ GeV and the total efficiency of central and forward region. Both Monte Carlo methods are in agreement within the statistical fluctuations. That means the muon weighting works

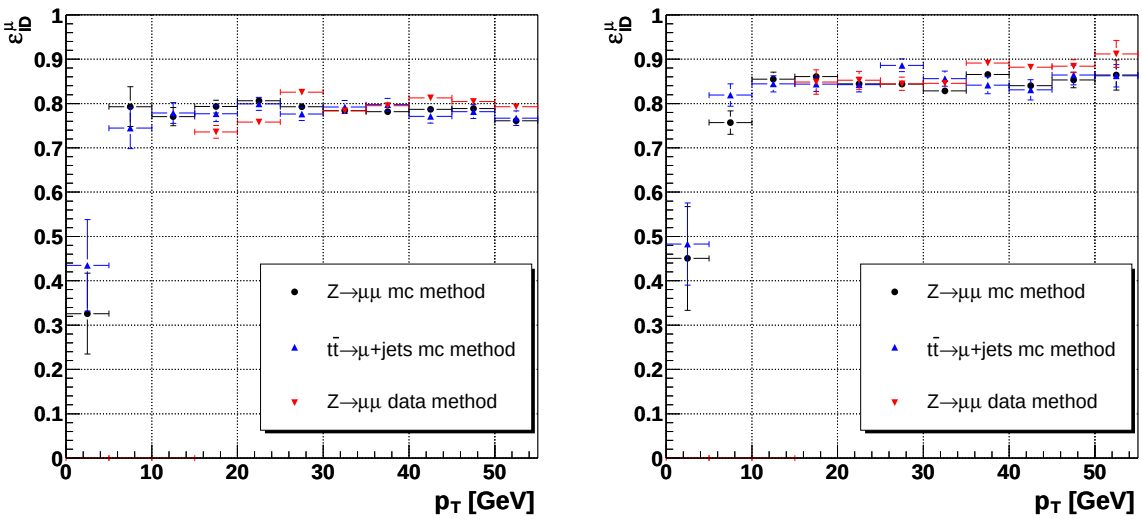

Figure 4.5: Muon identification efficiency $\varepsilon^{\mu}_{\mathrm{ID}}$ for $t\bar{t} \to \mu + \mathrm{jets}$ events versus transverse muon momentum determined with different methods in the central muon system (left) and the forward muon system (right).

correctly and has to be applied. The studies also show that the efficiencies would not agree without taking the different η-distributions of $t\bar{t} \to \mu + \mathrm{jets}$ and $Z \to \mu\mu$ events into account especially in the forward region . The data method seems to yield slightly higher efficiencies for muons with higher p_t. Nevertheless, this Monte Carlo study proofs that the data method is valid and provides correct results. The difference between $\varepsilon^{\mu}_{\mathrm{ID}}$ determined with the Monte Carlo and the data method is an estimation of the systematic uncertainty of the data method.

Method	Process	$\lvert\eta\rvert < 1.0$	$1.0 < \lvert\eta\rvert < 2.0$	$\lvert\eta\rvert < 2.0$
MC	$t\bar{t} \to \mu + \mathrm{jets}$	79.2 ± 0.4 %	86.0 ± 0.6 %	81.1 ± 0.3 %
MC	$Z \to \mu\mu$	78.7 ± 0.3 %	84.8 ± 0.5 %	80.6 ± 0.3 %
Data	$Z \to \mu\mu$	79.9 ± 0.3 %	87.1 ± 0.5 %	82.1 ± 0.3 %

Table 4.2: $\varepsilon^{\mu}_{\mathrm{ID}}$ determined with Monte Carlo and data method with simulated $t\bar{t} \to \mu + \mathrm{jets}$ and $Z \to \mu\mu$ events for the central, forward, and total muon detector region.

4.3.4 Distance of Closest Approach

One interesting question about a muon is whether it comes from the primary vertex or is the result of a particle decay at a secondary, displaced vertex. The "distance of closest approach", *dca* , helps answering this question. It is defined as the minimal distance of a muon track to the primary vertex in the transverse plane. The *dca* is not defined for muons without a match to an inner track. If no primary vertex is reconstructed it will be set to the detector center, but in this case the *dca* should not be used. The precision of measuring the muon track and the primary vertex is limited by the detector resolution causing an uncertainty in the *dca* . The *dca* divided by its uncertainty is called dca significance, σ_{dca} . Both variables will be investigated in four different simulated physics processes:

- $t\bar{t} \rightarrow \mu + \text{jets}$
- $W(\rightarrow \mu\nu) + \text{jets}$
- $Z \rightarrow \mu\mu$
- QCD multi jet events with high p_t muons ($p_t^{\mu} > 15$ GeV)

In the first three Monte Carlo samples the muon comes from the primary vertex, due to the extreme short lifetime of the top quark and the W or Z boson ($\tau \approx 10^{-25}$ s). In the Monte Carlo study the muon is explicitly required to originate from a W or Z boson decay and not from a semi-leptonic meson decay that might happen inside a jet. In contrast to that, the muon of the QCD sample comes from a secondary vertex. Hence, such muons are expected to have a large *dca*.
W + jets and QCD events are background processes for the $t\bar{t} \rightarrow \mu + \text{jets}$ signal events. The reason for analyzing $Z \rightarrow \mu\mu$ events is that their clear signature allows studies on data events as well as on Monte Carlo events. The comparison provides an estimate on how well the muon *dca* or σ_{dca} is simulated. For measurements with $Z \rightarrow \mu\mu$ data see [29]. Figure 4.6 shows the *dca* and σ_{dca} distributions of the muons for all samples. The *dca* distribution of $Z \rightarrow \mu\mu$, $t\bar{t} \rightarrow \mu + \text{jets}$, and W + jets events is quite similar, i.e. there is no difference between a muon originating from a Z, a W boson, or a top decay. As expected, the QCD sample distribution differs clearly from the others. In Figure 4.7 (a) the efficiency ε_{dca} of the cut $dca < x$ is plotted versus the cut position x. Figure 4.7 (b) is the same ($\varepsilon^{\sigma}_{\text{dca}}$) for the σ_{dca} . Comparing Figure 4.7 (a) and (b) it can be seen that a cut on the σ_{dca} is much more powerful than a cut on the *dca* for the W + jets and $Z \rightarrow \mu\mu$ sample. For the $t\bar{t} \rightarrow \mu + \text{jets}$ sample the σ_{dca} looks also more promising or is at least as good as a cut on the *dca* . The efficiency of the cut $\sigma_{\text{dca}} < 3$ is about 94% with a QCD background rejection of about 21%. Although ε_{dca} is almost the same for the first three samples there are significant differences in $\varepsilon^{\sigma}_{\text{dca}}$. This means that the uncertainty of the muon track and the primary vertex reconstruction differs in each physics process. $Z \rightarrow \mu\mu$ events have the smallest uncertainty.

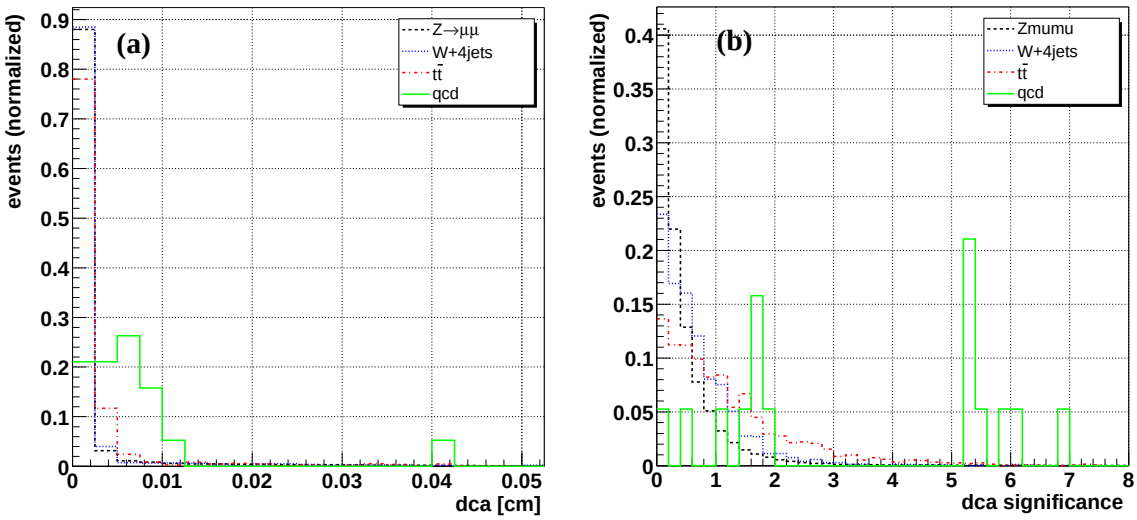

Figure 4.6: *Dca* (a) and σ_{dca} (b) distributions for different samples.

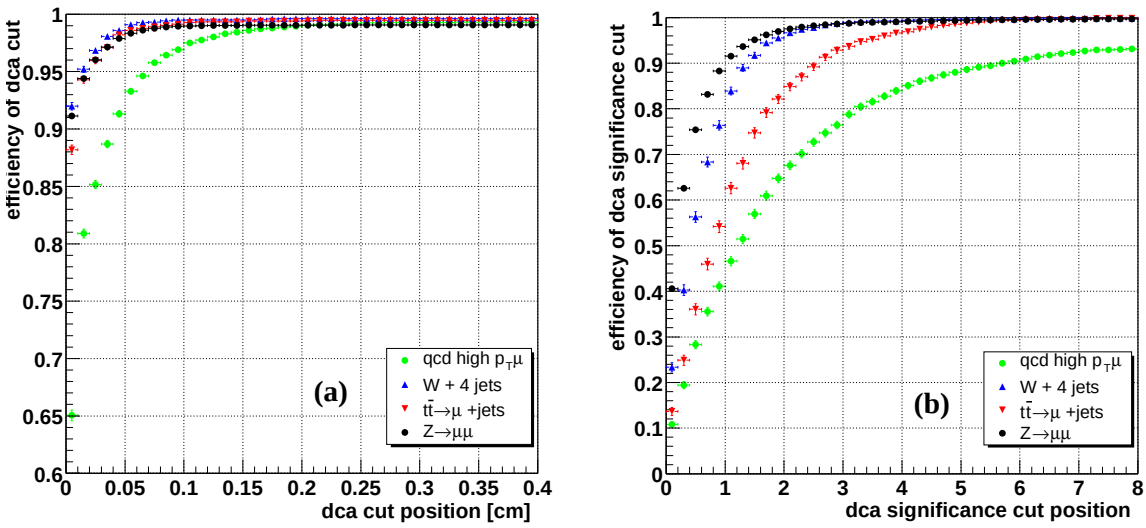

Figure 4.7: Efficiencies for cut on *dca* (a) and σ_{dca} (b) versus cut position for different samples.

This can be explained by the fact that most $Z \to \mu\mu$ events have no or only one jet. The less activity there is in the detector, the clearer hits are associated to the right tracks and a wrong identification of the primary vertex is less probable. $t\bar{t} \to \mu +$ jets events have typically four or more jets and therefore have a worse track resolution.
Due to Monte Carlo and data studies the $t\bar{t} \to \mu +$ jets analysis for the *Lepton Photon Conference 2003* [31] uses a σ_{dca} cut in the event preselection.

4.3.5 Muon Isolation

Muons from QCD events originate from semi-leptonic decays e.g. of bottom or charm mesons. Such muons can be discriminated from muons of e.g. a W or Z boson decay by the fact that they are inside of jets. Muons outside of jets are called isolated. The following section defines different isolation criteria and shows how the muon isolation for different physics processes can be determined.

Loose Isolation

The distance ΔR of the muon to the closest jet is a simple variable for an isolation criterion. Equation 4.5 gives the definition of "distance" and the so-called "loose isolation":

$$\Delta R(\mu, \text{jet}) = \sqrt{\Delta\eta^2 + \Delta\phi^2} > 0.5 \tag{4.5}$$

The value 0.5 corresponds to the cone size of jets (see the DØ jet definition in Section 4.1). The loose isolation cut rejects many QCD events, which is the reason why it is applied as preselection cut for the $t\bar{t} \to \mu +$ jets analysis. However, it fails if a jet with a muon inside is not reconstructed. The loose muon isolation is faked and more sophisticated criteria are necessary.

Tight Isolation

An improvement is achieved by considering calorimeter cells instead of reconstructed jets. The neighborhood or "halo" of a muon in the calorimeter is specified by a hollow cone with inner size R_a and outer size R_b as shown in Figure 4.8. The calorimeter halo E_t of a muon is the E_t sum of all calorimeter cells inside the muon halo:

$$\text{calorimeter halo } E_t = \sum_{R_i \in [R_a, R_b]} E_t^i.$$

Isolated muons in the calorimeter can be found by a cut on the calorimeter halo E_t. Similarly to the isolation in the calorimeter a muon isolation in the tracker can be defined. Summing up all track p_t of all tracks in a cone of size R_c around the muon without taking the muon track yields the tracker halo p_t:

$$\text{tracker halo } p_t = \sum_{R_i < R_c} p_t^i.$$

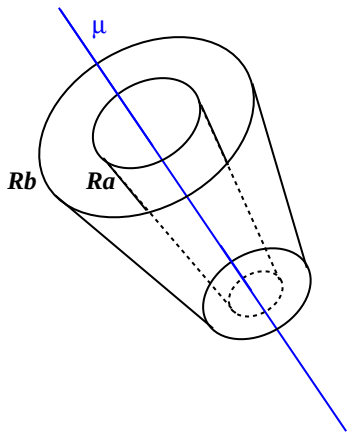

Figure 4.8: Muon halo, i.e. hollow cone around the muon in the calorimeter

The "tight isolation" of a muon is a combination of isolation in the calorimeter and the tracker. A tight isolated muon fulfills:

$$\text{calorimeter halo } E_t < 2.5 \text{ GeV} \quad \text{and} \quad \text{tracker halo } p_t < 2.5 \text{ GeV},$$

whereas the cone sizes are given by:

$$R_a = 0.1 \qquad R_b = 0.4 \qquad R_c = 0.5.$$

Isolation Efficiency

The muon isolation efficiency is the ratio of tight isolated muons and the total number of muons. In Section 5.2 the matrix method will be described. It discriminates QCD events from W + jets events including $t\bar{t} \rightarrow \mu +$ jets events and relies on different muon isolation efficiencies of the two processes. This section describes how to measure the muon isolation efficiency for QCD events, ε^{QCD}, and for $t\bar{t} \rightarrow \mu +$ jets and W + jets events, ε^{sig}. It is important to measure these efficiencies using data and not simulated events, because the fragmentation models that simulate jets cannot describe data jets with the required accuracy. The muon isolation efficiency ε^{sig} is the same for $t\bar{t} \rightarrow \mu +$ jets events and for W + jets events. Therefore, the muon isolation cannot be used distinguish those two processes, i.e. the matrix method will only discriminate QCD background from signal.

Isolation Efficiency of Signal events

The signal muon isolation efficiency ε^{sig} cannot be measured in a $t\bar{t} \rightarrow \mu +$ jets data sample, because $t\bar{t} \rightarrow \mu +$ jets events cannot be identified without cutting on the muon isolation. Hence, ε^{sig} is determined using simulated $t\bar{t} \rightarrow \mu +$ jets events. However,

the muon isolation can also be measured using $Z \to \mu\mu$ data events as is demonstrated below using Monte Carlo events. Comparing the results of the $Z \to \mu\mu$ data method with a measurement that uses simulated $Z \to \mu\mu$ events gives an estimate on how well the isolation is described by the simulation. The $Z \to \mu\mu$ data events are identified by two reconstructed muons, that fly back-to-back with a di-muon mass at the Z-peak. This is similar to the data method for the muon identification. The muon isolation is tested for each muon in a $Z \to \mu\mu$ sample to obtain the muon isolation efficiency. Muons coming from a Z-boson or a W-boson decay have almost the same properties, but the jets of $Z \to \mu\mu$ and $t\bar{t} \to \mu +$ jets events differ in their E_t- and η-distributions. Jets of $t\bar{t} \to \mu +$ jets events are harder and more central than jets of $Z \to \mu\mu$ events, which are mainly produced by gluon radiation. For this reason the isolation efficiency measured with $Z \to \mu\mu$ data is only used for an estimation of the systematic uncertainty of the simulations.
It is not surprising, that $t\bar{t} \to \mu +$ jets and W + jets events have the same isolation efficiency. In a way $t\bar{t} \to \mu +$ jets events are W + jets events with the difference that the W arises from a top quark decay. Indeed, the agreement of the efficiencies of both processes can be confirmed with Monte Carlo events.
The muon isolation efficiency is a function of the inclusive jet multiplicity. The more jets there are in an event the higher is the probability for a muon to be not isolated. Therefore, $\varepsilon^{\mathrm{sig}}$ is determined for each jet multiplicity separately.

Isolation Efficiency of QCD background events

To measure the muon isolation efficiency $\varepsilon^{\mathrm{QCD}}$ for muons of QCD events an enriched QCD data sample with a high p_t muon has to be created. In order to do this an event with muon $p_t > 15$ GeV, $\not{E}_t < 15$ GeV, and calorimeter $\not{E}_t < 25$ GeV is requested. The missing transverse energy cuts exclude events with a W-boson decaying in muon and neutrino with large transverse momentum. Thus, $\varepsilon^{\mathrm{QCD}}$ can be determined completely independent of simulations. However, the QCD background which is relevant for $t\bar{t} \to \mu +$ jets events passes a preselection that requires large missing transverse energy ($\not{E}_t > 20$ GeV). Hence, it has to be investigated whether the muon isolation efficiency depends on $\not{E}_t$, i.e. the $\varepsilon^{\mathrm{QCD}}$ determined in the data QCD sample with $\not{E}_t < 15$ GeV is representative for QCD background events with $\not{E}_t > 20$ GeV. This question is addressed in a Monte Carlo study. The study uses the p13 QCD Monte Carlo sample with high p_t muons, that is also used for the *dca* studies. Most events contain only one jet, thus a dependence on the jet multiplicity cannot be tested. Figure 4.9 shows $\varepsilon^{\mathrm{QCD}}$ versus $\not{E}_t$ for events with a muon with $p_t > 15$ GeV. First of all it can be seen that there are only a few events with high $\not{E}_t$. Although the statistics is too low to conclude something for the range with $\not{E}_t$ >15 GeV, there seems to be a tendency that the muon isolation efficiency drops with increasing $\not{E}_t$.
In order to study the isolation efficiency with the simulation, the Monte Carlo sample must represent the data. However, looking at the origin of the muons yields that the

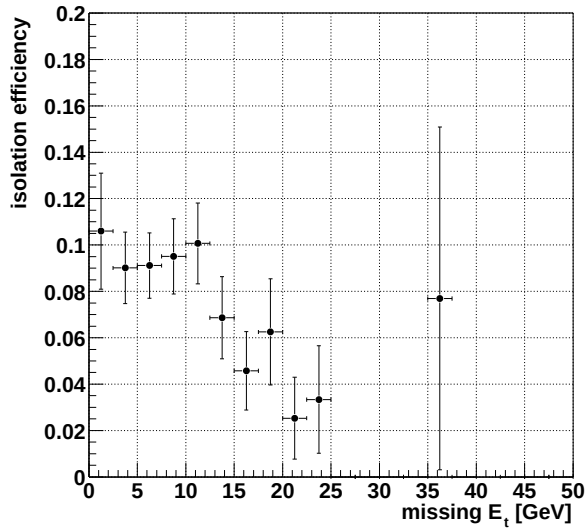

Figure 4.9: Muon isolation efficiency vs. $\not{E}_t$ for simulated QCD events containing a muon with $p_t^\mu > 15$ GeV.

simulated QCD sample is highly dominated by muons from semi-leptonic b-decays, i.e. muons from e.g. pions, strange or charmed hadrons, and taus are neglected.
With the available events the origin of the missing transverse energy is investigated. This might give a hint on different mechanisms that lead to a fake muon isolation for small and large $\not{E}_t$. Figure 4.10 (a) shows the neutrino E_t of the neutrino coming from the semi-leptonic decay, and the $\not{E}_t$ spectrum. It is obvious, that the neutrino is not the only source of $\not{E}_t$. Figure 4.10 (b) shows the angle in the transverse plane between the leading jet and the missing transverse energy for $\not{E}_t > 10$ GeV and $\not{E}_t < 10$ GeV. The leading jet of most events is back-to-back to the missing transverse energy. This happens in di-jet events, where one jet is not reconstructed. Jets that are not reconstructed cannot be energy scale corrected which leads to missing energy. This seems to happen more often in events with $\not{E}_t > 10$ GeV.
A final conclusion on the impact on the muon isolation cannot be given, because the number of events with an isolated muon and large missing transverse energy is too low.

The study also investigates how the QCD background can be further suppressed. Therefore, the transverse mass, m_t, is considered:

$$m_t = \sqrt{(E_t^\mu + E_t^\nu)^2 - (\vec{p}_t^\mu + \vec{p}_t^\nu)^2} \approx \sqrt{2E_t^\mu E_t^\nu (1 - \cos\Delta\phi(\mu,\nu)}. \tag{4.6}$$

The right part of Equation 4.6 is obtained neglecting the muon and neutrino mass. It gives the relation of m_t and the angle $\Delta\phi(\mu,\nu)$ between the muon and the neutrino. In

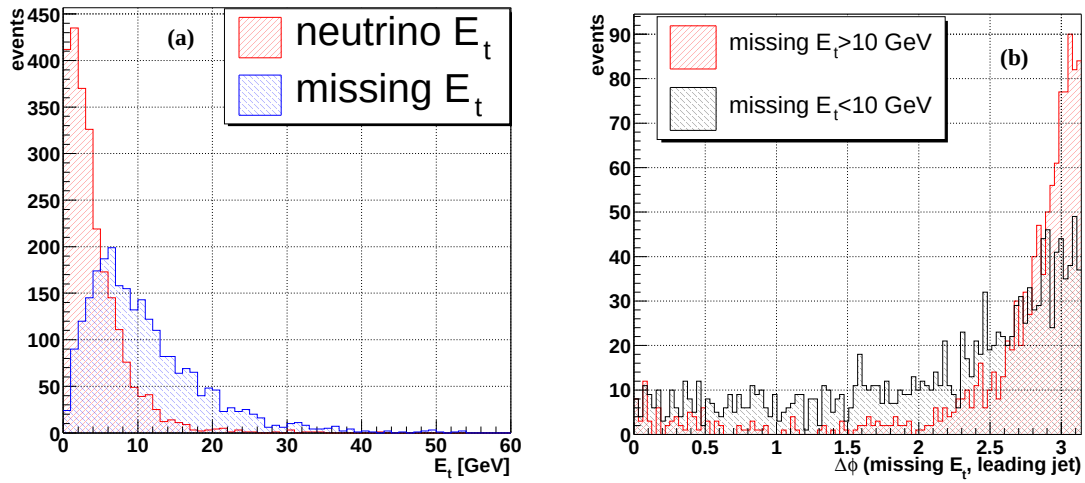

Figure 4.10: Transverse energy of the neutrino and missing transverse energy in simulated QCD with a muon ($p_t^\mu > 15$ GeV) (a) and distribution of the angle $\Delta\phi$ between $\not{E}_t$ and the leading jet for events with low and high $\not{E}_t$ (b).

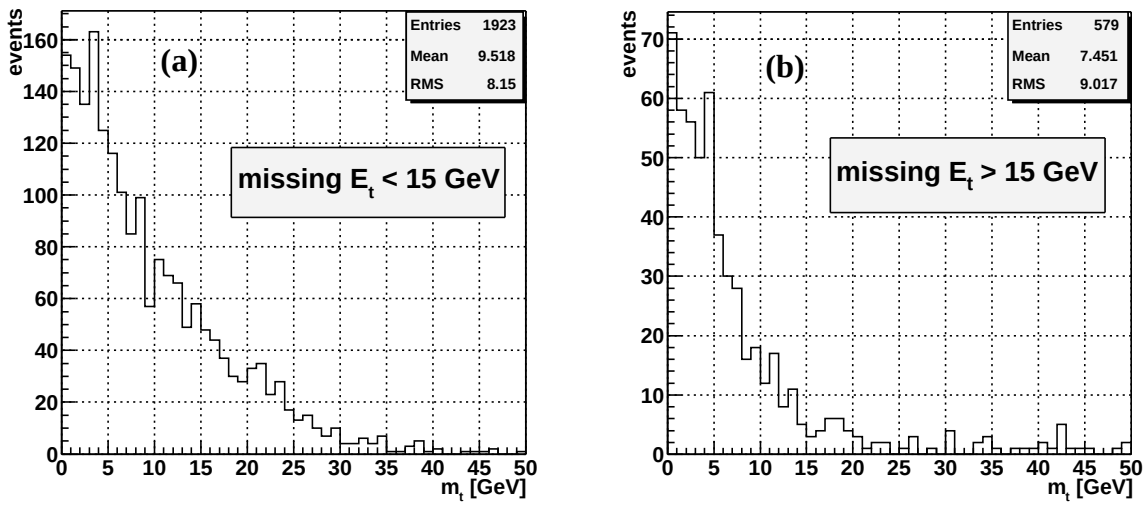

Figure 4.11: Transverse mass distribution for QCD events with low (a) and high (b) missing transverse energy.

W + jets events m_t is the transverse mass of the W boson, i.e. the m_t distribution peaks at the W mass. Figure 4.11 shows the m_t distribution for QCD events for small (a) and large (b) missing transverse energy. Both distributions peak at zero, but the higher the missing energy, the smaller the width of the peak. Indeed, the data analysis for the next winter conference includes a so-called triangle cut. This is a two-dimensional cut depending on $\not{E}_t$ and $\Delta\phi(\mu,\not{E}_t)$, based on a study with data [32].

5 Monte Carlo Cross Section

In this chapter the analysis of $t\bar{t}$ production in the muon + jets channel is discussed. Ways of extracting the signal, the preselection, and two methods to estimate the contribution of QCD and W + jets background are described. The analysis steps to measure the $t\bar{t}$ production cross section with simulated events are performed. The final step of the measurement is the analysis of the preselected events. The different event topologies of signal and background events is used to separate a candidate sample. As a result there will be a measurement of the $t\bar{t}$ production cross section and its uncertainty as a function of the simulated cross section and integrated luminosity. The systematic uncertainties and results will be discussed in the Chapter 6.

5.1 Preselection

The very first step of the analysis is the preselection. Its aim is the selection of events with a muon and a neutrino coming from a W boson. Signal events should pass the preselection cuts with a high efficiency, whereas the contribution from QCD background events is reduced. The preselection cuts are taken from the analysis presented at the *Lepton Photon Conference 2003* [31]. The preselection cuts and their efficiencies are described in detail below. All efficiencies are given with respect to the cuts, that were applied before. The total efficiency of the preselection is the product of all relative efficiencies:

$$\varepsilon_{\text{preselection}} = \prod_i \varepsilon_i. \tag{5.1}$$

A summary is given in Section 5.1.11. The following sections discuss all preselection requirements.

5.1.1 Muon Identification

Only medium muons are used in the analysis. The way to measure the identification efficiency for medium muons is discussed in Chapter 4.3.3. The identification efficiency times acceptance of the $t\bar{t} \to \mu +$ jets events is found to be:

$$\varepsilon^{\mu}_{ID} \times \text{acceptance} = 65.0 \pm 0.8\% \,(\text{stat}).$$

5.1.2 Muon Tracking

In addition to the medium quality criteria all in the muon system identified objects are matched to a track in the central tracking system. There was a significant improvement of the tracking algorithm from the p13 software to the p14 version. The muon track matching efficiency is the efficiency to reconstruct a track in the inner tracking system times the efficiency to match it to the reconstructed object in the muon system. In the data analysis the muon track matching efficiency is measured with a sample of $Z \to \mu\mu$ events. The test sample contains two medium muons. To identify the $Z \to \mu\mu$ events a minimum cut on $\Delta\phi(\mu, \mu)$ and a cut on the di-muon mass is applied. Both transverse muon momenta are measured with the local muon system and are required to be greater than 15 GeV. The track matching efficiency is the ratio of number of muons with track match and twice the number of di-muon events. The efficiency is measured as a function of the muon η and convoluted with the expected muon η distribution in $t\bar{t} \to \mu + \text{jets}$ events. For the data measurements see [29].
In Monte Carlo the muon track matching efficiency is determined with simulated $t\bar{t} \to \mu + \text{jets}$ events. The efficiency to match a medium muon to a central track is found to:

$$\varepsilon^{\mu}_{\text{track}} = 96.5 \pm 0.4\% \,(\text{stat}).$$

5.1.3 Loose Isolation

The loose muon isolation is introduced in Section 4.3.5. The cut on the distance between muon and nearest jet $\Delta R(\mu, \text{jet}) > 0.5$ rejects many QCD background events with a muon coming from a semi-leptonic decay inside a jet. Figure 5.1 (a) shows the $\Delta R(\mu, \text{jet})$ distribution for simulated $t\bar{t} \to \mu + \text{jets}$ events. The signal efficiency of the loose isolation is measured to be:

$$\varepsilon_{\Delta R} = 84.2\% \pm 0.5\% \,(\text{stat}).$$

In [29] it is shown, that there is a good agreement in loose isolation efficiency determined with $Z \to \mu\mu$ data and simulated $Z \to \mu\mu$ events. Therefore, in [29], $\varepsilon_{\Delta R}$ is also determined with simulated $t\bar{t} \to \mu + \text{jets}$ events.

5.1.4 Transverse Muon Momentum

Signal muons have a large transverse momentum, because they are the decay products of real W bosons. The preselection cut, $p_t^{\mu} > 20$ GeV, reduces background with soft muons. The signal efficiency is measured to:

$$\varepsilon^{\mu}_{p_t} = 88.0 \pm 0.8\% \,(\text{stat}).$$

The muon p_t spectrum is shown in Figure 5.1 (b). In the data analysis this efficiency is also taken from the simulation, but the Monte Carlo muon p_t is smeared in order to correspond to the data resolution [33].

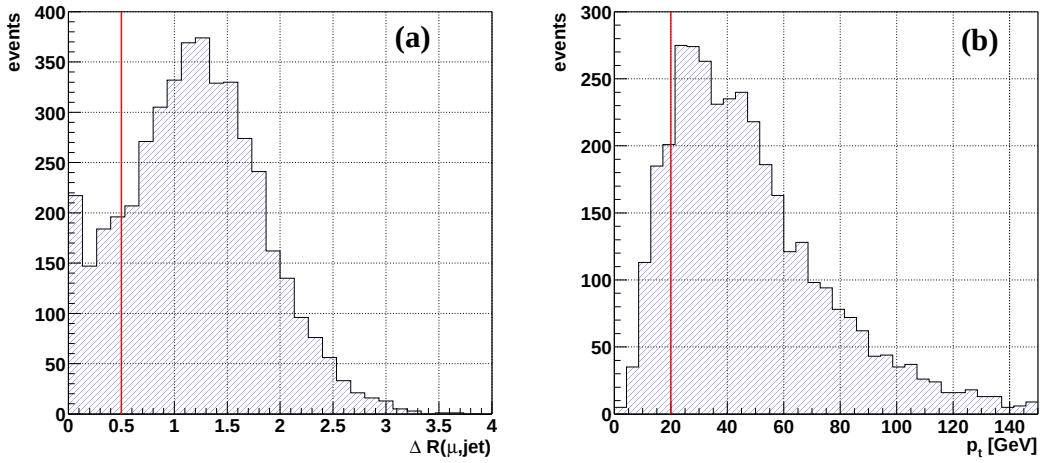

Figure 5.1: Distance between muon and next jet $\Delta R(\mu, \text{jet})$ (a) and muon p_t spectrum for simulated $t\bar{t} \to \mu + \text{jets}$ events (b).

5.1.5 Primary Vertex

In order to be able to use the muon σ_{dca}, described in Section 4.3.4, it is necessary to require the reconstruction of the primary vertex. A primary vertex reconstruction is only possible with at least two tracks. The standard primary vertex quality cuts of the DØ Top Group are a requirement of more then two tracks, and a vertex z position of $|z| < 60$ cm, to be in the fiducial region of the tracking system. Figure 5.2 (a) and (b) show the distributions and cut positions of both variables. If there is no reconstructed primary vertex the number of associated tracks is set to zero. The obtained efficiency for both requirements is:

$$\varepsilon_{PV} = 98.3 \pm 0.3\% \,(\text{stat}).$$

Since the performance of the tracking in the p13 reconstruction version is not simulated well, the data analysis used W + jets and QCD enriched data samples to determine the primary vertex reconstruction efficiency.

5.1.6 Muon Significance of the Distance of Closest Approach

The muon of a $t\bar{t} \to \mu$+jets event comes from the primary vertex. Therefore, the *dca* (see Section 4.3.4) should be zero within its uncertainty. To distinguish between signal muons coming from the primary vertex and muons from secondary displaced vertices the cut $\sigma_{\text{dca}} < 3$ is applied. Section 4.3.4 describes how the efficiency has been determined. In

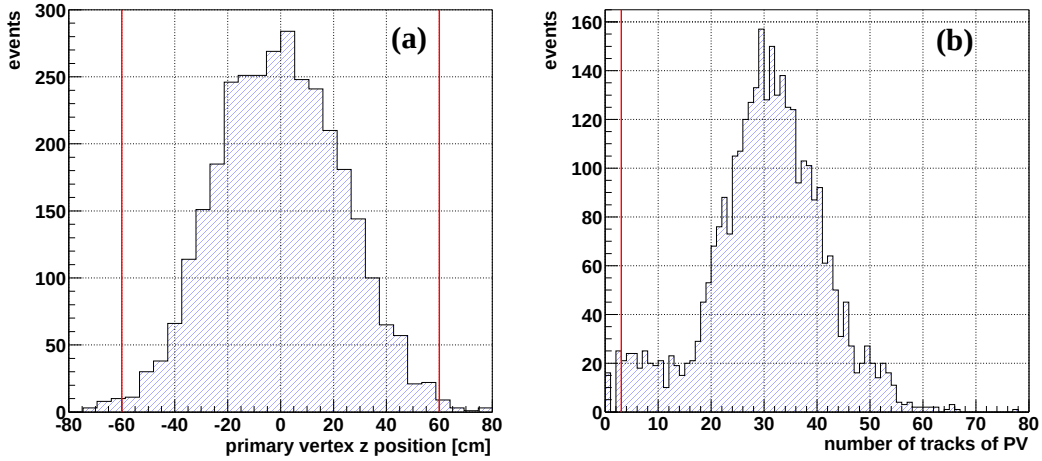

Figure 5.2: Primary vertex z-position (a) and associated number of tracks (b) for simulated $t\bar{t} \to \mu +$ jets events.

the Monte Carlo study it is found to be:

$$\varepsilon^{\mu}_{\text{dca}} = 96.7 \pm 0.4\% \text{ (stat)}.$$

5.1.7 Muon Trigger

Recorded $t\bar{t} \to \mu +$ jets events have to be triggered by the muon trigger. Figure 5.3 shows the measurement of the muon trigger efficiency as a function of η for Level 1 and Level 2. The asymmetry in η is caused by different detector inefficiencies for positive and negative η. The results are taken from [29]. Trigger inefficiencies are determined with the help of independent triggers. Both trigger curves are parameterized as a function of η. These parameterizations are used to simulate the trigger in Monte Carlo events. The efficiency is considered as probability for an event to be triggered. Each event is weighted by this probability. The muon η-distribution of the $t\bar{t} \to \mu +$ jets events is convoluted with the product of the muon trigger parametrizations for the Level 1 and Level 2 trigger. In [29] the combined Level 1 and 2 muon trigger efficiency was found to be:

$$\varepsilon^{\mu}_{\text{trigger}} = 88.7 \pm 1.4\%,$$

where the uncertainty is a combined statistical and systematic uncertainty.
Of course, only triggered data can be analyzed offline. But in the Monte Carlo study the order of applying cuts and introducing trigger weights is not important, because the total efficiency remains unchanged.

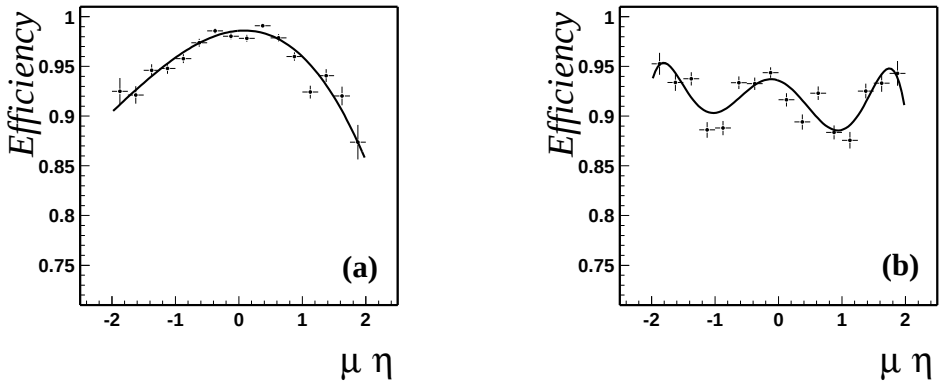

Figure 5.3: Measurements and parametrizations of the Level 1 (a) and Level 2 (b) muon trigger as a function of the muon η, from [29].

5.1.8 Jet Identification and Jet Multiplicity

The efficiency to reconstruct jets in the calorimeter also enters the total efficiency and therefore the cross section. See Section 4.1 for the jet identification criteria and Section 4.1.2 for an explanation of how the jet identification efficiency is measured with data. The final sample with the $t\bar{t} \to \mu +$jets candidate events contains only events with four or more jets. The cut $N_{\text{jets}} \geqslant 4$ is not part of the preselection, but will be applied later. The method to estimate the background contribution from QCD events, that will be described in 5.2 and 5.3, is performed for all jet multiplicities. For the Monte Carlo study the jet identification efficiency times the efficiency of the cut on N_{jets} is determined in one step with simulated $t\bar{t} \to \mu +$ jets events. In addition to the jet identification criteria the $t\bar{t}$ analysis uses only jets with a jet $E_t > 15$ GeV and only central jets are used in the analysis ($|\eta_{\text{jet}}| < 2.5$). Figure 5.6 (a) shows the jet multiplicity of simulated $t\bar{t} \to \mu +$jets events. The efficiency of the jet identification, the N_{jets}, jet E_t, and η_{jet} cut is obtained to be:

$$\varepsilon_{\text{Njets}} \times \varepsilon_{\text{ID}}^{\text{jet}} = 62.1 \pm 0.8\% \,(\text{stat}).$$

5.1.9 Jet Trigger

Besides the muon trigger the events must be selected by the jet trigger. Figure 5.4 and Figure 5.5 (a) show the data measurements and parameterizations of the Level 1 and two Level 3 jet triggers. The Level 1 jet trigger is called CJT(1,5) and the Level 3 jet trigger is called JET(1,20,3), where Figure 5.4 (a) and (b) show the trigger with a 1.5 σ

and a 2.5 σ zero suppression, respectively (see [29]). These triggers were used to record the data for the *Lepton Photon 2003* analysis [31, 29].

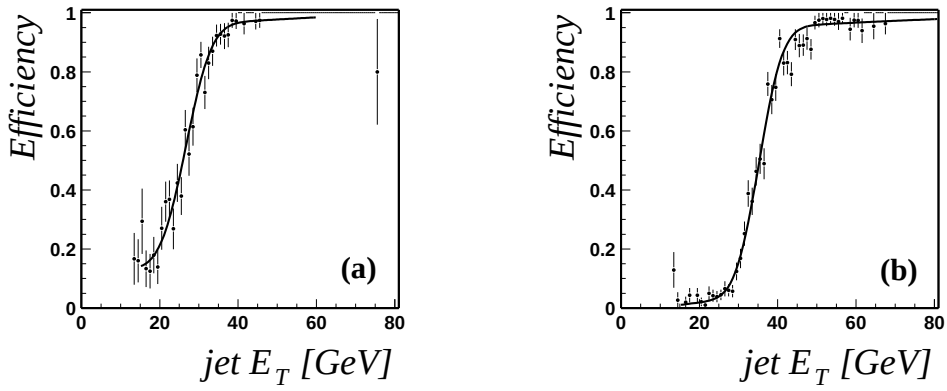

Figure 5.4: Level 3 jet trigger efficiency turn-on curves as a function of E_t for 1.5 σ (a) and 2.5 σ (b) zero suppression [29].

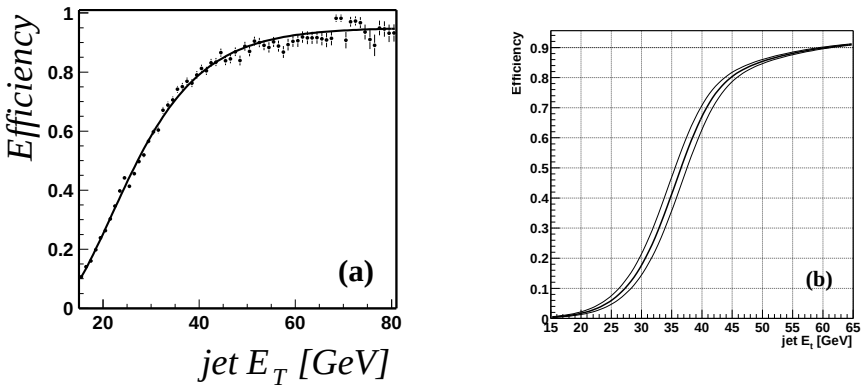

Figure 5.5: Level 1 jet trigger efficiency turn-on curve as a function of E_t (a), [29] and the combined trigger efficiency of Level 1 and 3, and the range in which the turn-on curve is varied (b).

For the Monte Carlo study the trigger curves are used to calculate event weights to simulate the effect of the jet trigger. The efficiencies are parameterized by E_t, but the η-dependence is not considered here. Within the data taking period analyzed in [29] the Level 3 jet trigger was changed. The turn-on curve shown in Figure 5.4 (b) represents one third of the total data sample, while two third were recorded with the Level 3 jet trigger resulting the turn-on curve shown in 5.5 (a). Therefore, the probability for a jet to fire the trigger is calculated by:

$$\varepsilon^{\text{jet}}_{\text{trigg}}(E_t^{\text{jet}}) = \varepsilon_{\text{Level 1}}(E_t^{\text{jet}}) \times [\frac{1}{3} \cdot \varepsilon^{(a)}_{\text{Level 3}}(E_t^{\text{jet}}) + \frac{2}{3} \cdot \varepsilon^{(b)}_{\text{Level 3}}(E_t^{\text{jet}})] \tag{5.2}$$

Equation 5.2 combines both Level 3 triggers and the Level 1 trigger. Figure 5.5 (b) shows the resulting curve of all jet trigger level. With increasing number of jets in an event, the probability for the event to be recorded increases.
The weight w of an event with N_{jets} jets is given by:

$$w = 1 - \prod_{i=1}^{N_{\text{jets}}} \left[1 - \varepsilon^{\text{jet}}_{\text{trigg}}(E_t^{\text{jet}_i}) \right]. \tag{5.3}$$

In the data analysis as well as in the Monte Carlo study the jet trigger efficiency for $t\bar{t} \to \mu +$ jets events with at least four jets is determined with the simulated jet E_t spectrum. The efficiency is obtained by summing up all event weights divided by the number of $t\bar{t} \to \mu +$ jets events. There are uncertainties of the trigger parameterization. The measured data points fluctuate statistically and there is an uncertainty due to the choice of an appropriate fit function. To estimate these effects the jet trigger efficiency is also determined with trigger curves, where the trigger threshold is shifted by ± 1 GeV. Figure 5.5 (b) shows the combined Level 1 and Level 3 turn-on curves and includes the shifted curves. The result is:

$$\varepsilon^{\text{jet}}_{\text{trigger}} = 99.7 \pm 0.1\% \text{ (syst)}.$$

The jet trigger weights are multiplied to the muon trigger weights.

5.1.10 Missing Transverse Energy

Also the neutrino has a large transverse momentum. The presence of such a neutrino is indirectly observed by missing transverse energy, $\not{E}_t$. In Figure 5.6 (b) the $\not{E}_t$ spectrum of simulated $t\bar{t} \to \mu +$ jets events can be seen. The preselection requirement is chosen to be $\not{E}_t > 20$ GeV. Data analysis and Monte Carlo study determine the efficiency from the simulation. It is found to be:

$$\varepsilon_{\not{E}_t} = 90.9 \pm 1.1\% \text{ (stat)}.$$

In [29] the efficiency is also studied with $Z \to \mu\mu$ data. Systematic uncertainties coming from the jet energy scale correction are discussed in Chapter 6.

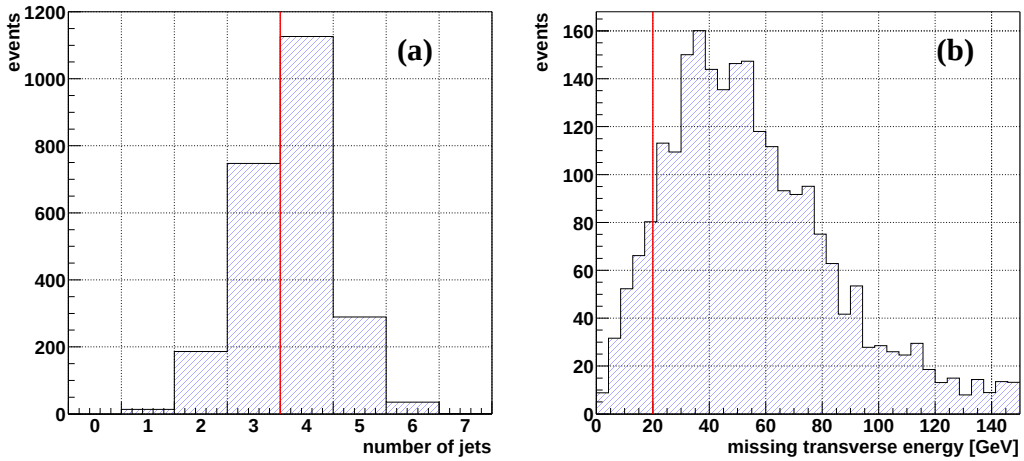

Figure 5.6: Distribution of the jet multiplicity (a) and the missing transverse energy spectrum (b) of simulated $t\bar{t} \to \mu + \text{jets}$ events.

5.1.11 Summary of all Preselection Cuts

All preselection requirements with their signal efficiencies are summarized in Table 5.1. The total preselection efficiency is calculated with Equation 5.1 and its uncertainty is given by Gaussian error propagation. In the preselection of the *Lepton Photon Confer-*

Efficiency	Value	Comment
$\varepsilon^{\mu}_{\text{ID}} \times$ acceptance	65.0 ± 0.8 %	medium muon
$\varepsilon^{\mu}_{\text{track}}$	96.5 ± 0.4 %	muon track
$\varepsilon^{\mu}_{\Delta R}$	83.4 ± 0.8 %	$\Delta R(\mu, \text{jet}) > 0.5$
$\varepsilon^{\mu}_{p_t}$	88.0 ± 0.8 %	muon $p_t > 20$ GeV
ε_{PV}	98.0 ± 0.3 %	primary vertex
$\varepsilon^{\mu}_{\text{dca}}$	96.7 ± 0.4 %	muon $p_t > 20$ GeV
$\varepsilon^{\mu}_{\text{isolation}}$	90.2 ± 0.8 %	tight muon isolation
$\varepsilon^{\mu}_{\text{trigger}}$	88.7 ± 1.4 %	muon trigger
$\varepsilon_{\text{Njets}} \times \varepsilon^{\text{jet}}_{\text{ID}}$	62.1 ± 0.8 %	$N_{\text{jets}} \geqslant 4$, jet ID
$\varepsilon^{\text{jet}}_{\text{trigger}}$	99.7 ± 0.1 %	L1, L3 jet trigger
$\varepsilon_{\not{E}_t}$	90.9 ± 1.1%	$\not{E}_t > 20$ GeV
$\varepsilon_{\text{preselection}}$	19.2 ± 0.6%	

Table 5.1: Efficiencies of preselection cuts for $t\bar{t} \to \mu + \text{jets}$ sample.

ence 2003 [31] analysis, there was in addition a soft muon veto on a second muon in $t\bar{t} \to \mu +$ jets events that is not applied in this Monte Carlo study. Note, that although the $N_{\text{jets}} \geqslant 4$ cut is listed in the preselection, the following analysis steps are performed for all jet multiplicities. That will be necessary for the Berends Scaling method, described in Section 5.3.

5.2 Matrix Method

The first step of background reduction is aimed at the QCD background. Separating background with the matrix method relies on the different muon isolation efficiencies for muons from a W boson decay or QCD background. The method separates QCD events from $t\bar{t} \to \mu +$ jets and W + jets events. Two samples are defined, a "loose sample" consisting of all events surviving the preselection cuts including the loose muon isolation cut, and a sample called "tight sample" which is a subset of the loose sample. It contains only events with tightly isolated muons, i.e. the muons pass the tight isolation criteria defined in Section 4.3.5. This yields the following matrix equation (or linear system of equations):

$$\begin{aligned} N_{\text{loose}} &= N^{t\bar{t}+W} + N^{\text{QCD}} \\ N_{\text{tight}} &= \varepsilon^{\text{sig}} \cdot N^{t\bar{t}+W} + \varepsilon^{\text{QCD}} \cdot N^{\text{QCD}}, \end{aligned}$$

where ε^{sig} is the tight muon isolation efficiency for $t\bar{t} \to \mu +$ jets and W + jets events to get from the loose to the tight sample and ε^{QCD} is the muon isolation efficiency for QCD events. ε^{sig} is the same for $t\bar{t} \to \mu +$ jets and W + jets events due to the same origin of the muons. The measurement of ε^{sig} and ε^{QCD} is described in Section 4.3.5. The matrix method uses only information extracted from data, as N_{loose}, N_{tight}, ε^{sig}, and ε^{QCD} can all be measured with data. This is essential since it is not possible to simulate jets and muon isolation with the desired accuracy. The hadronization of partons cannot be calculated perturbatively, but is described by fragmentation models. To measure the muon isolation efficiency with Monte Carlo events an exact fragmentation model for heavy flavor jets is needed. Moreover, the cross section uncertainty of the inclusive jet production is large. The simulation of the calorimeter response and detector noise even increase the uncertainty, which makes the use of Monte Carlo events questionable. Nevertheless, it would be reassuring to cross check the matrix method with Monte Carlo events. However, there are not enough QCD multijet Monte Carlo events available. It would require to generate several million multijet QCD events, given the small preselection efficiency on QCD background and the small value of ε^{QCD}, see also Section 3.3. Note that the measurement of the $t\bar{t}$ production cross section in Monte Carlo without having QCD background impacts the estimation of the number of background events. This will not be taken into account in the estimation of the systematic uncertainty.

To illustrate the effect of the matrix method Figure 5.7 (taken from [34]) shows the separated QCD fraction (a) and the W + $\geqslant$ 4 jets with $t\bar{t} \rightarrow \mu + \geqslant 4$ jets fraction (b) for data as a function of the transverse mass. The transverse mass is reconstructed by the transverse muon momentum and missing transverse energy. All distributions are in agreement with simulated distributions, that are normalized to the same number of events. As expected, the transverse mass of QCD background is small, whereas for the W + jets and $t\bar{t} \rightarrow \mu +$ jets events the transverse mass distribution peaks at the W boson mass.

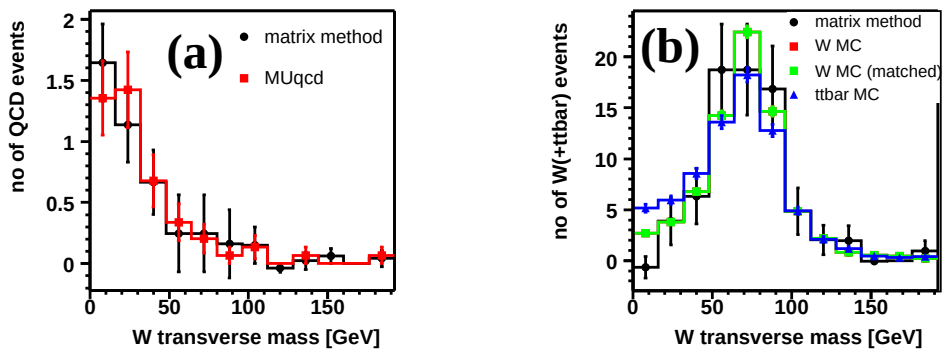

Figure 5.7: Transverse mass distributions for QCD (a), W+jets, and $t\bar{t} \rightarrow \mu +$ jets (b) events with four or more jets after the separation by the matrix method, from [32, 34].

5.3 Berends Scaling

The matrix method provides an estimate on the number of QCD events. Estimating the W + jets background is the next step. The idea of the W + jets background estimation is based on Berends empirical scaling law. According to the Berends Scaling the number of W + n jets events with n or more jets decreases by a factor of α with increasing inclusive jet multiplicity n:

$$\frac{\sigma(W + (n+1)_{\text{jets}})}{\sigma(W + n_{\text{jets}})} = \alpha.$$

This assumption can be explained by the fact, that every additional jet originates from a parton with an additional vertex factor $\sqrt{\alpha_s}$, where α_s is the strong coupling constant (see Feynman graphs in Figure 2.7). Hence, the cross section decreases by α_s ignoring

higher order corrections. The value of the constant α depends on cuts on the parton p_t and η and the minimal distance between two partons ΔR. Indeed, α is found to be of the order of α_s, $\alpha_s(M_Z) = 0.1172(20)$ [18].
Applying the matrix method for each inclusive jet multiplicity i separately, i tight samples are obtained. The number of observed events, $N_i^{W+t\bar{t}}$, versus the jet multiplicity i is an exponentially decreasing distribution of the W + jets events with the superimposed jet multiplicity distribution of the $t\bar{t} \to \mu$+jets events. Most $t\bar{t} \to \mu$+jets events contain four or more jets. The relative $t\bar{t}$ fraction is largest for jet multiplicity greater or equal four. According to Berends scaling the jet multiplicity distribution can be fitted by the following equation:

$$N_i^{W+t\bar{t}} = N_1^W \times \alpha^{i-1} + f_i^{t\bar{t}} N^{t\bar{t}}. \tag{5.4}$$

N_i^W is the number of W + jets events in bin i, α is a constant, and $N^{t\bar{t}}$ is the number of $t\bar{t}$ events. These are the fit parameters. The factors $f_i^{t\bar{t}}$ give the fraction of $t\bar{t}$ events in each multiplicity bin measured with simulated events. The fit result for $N_1^W$is dominated by the high statistics of the first bins, but the result for $N^{t\bar{t}}$ is not significant and will not be used for the further analysis. Only the background in the fourth bin, N_4^W is estimated:

$$N_4^W = N_1^W \times \alpha^3. \tag{5.5}$$

The Berends Scaling method provides an estimation of the number of W + 4 jets background events of the total number of observed events in the fourth jet multiplicity bin after the preselection is applied.

Trigger Bias

All measured events are triggered by the jet trigger. The measured jet E_t spectrum differs from the spectrum in the simulation due to the trigger inefficiency. The resulting samples are called "biased", because they depend on the trigger and do not represent the original or "unbiased" sample. The effect of the bias differs for each jet multiplicity, since the probability for an event to be triggered increases with increasing jet multiplicity (see Equation 5.3). Figure 5.8 shows the biased and unbiased $t\bar{t} \to \mu +$jets events (a) and W + jets events (b) for each inclusive jet multiplicity. Note, that the jet trigger for $t\bar{t} \to \mu +$jets events with four or more jets is 99.7% efficient. Berends scaling is valid for unbiased distributions. In order to apply the Berends scaling method, the trigger bias has to be corrected. To obtain the unbiased number of events $N_i^{W+t\bar{t}}$ in each bin i, the number of biased observed events $\tilde{N}_i^{W+t\bar{t}}$ has to be corrected by the bias $\varepsilon_i^{\text{bias}}$:

$$N_i^{W+t\bar{t}} = \frac{1}{\varepsilon_i^{\text{bias}}} \cdot \tilde{N}_i^{W+t\bar{t}}. \tag{5.6}$$

In data the trigger biases $\varepsilon_i^{\text{bias}}$ are measured with a jet independent trigger, namely the single muon trigger. The effects of the muon trigger or the preselection requirements do not have to be corrected, because they do not have an impact on the jet multiplicity

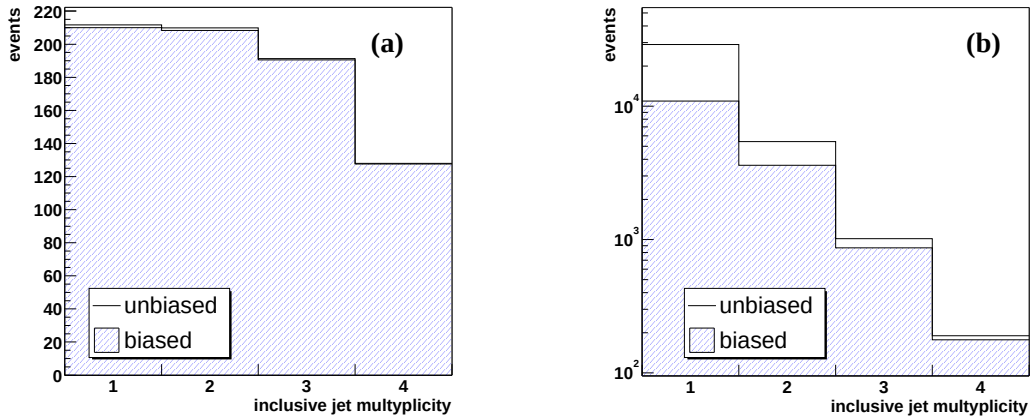

Figure 5.8: Simulated trigger bias for $t\bar{t}$ (a) and W + jets (b) events.

distribution. Section 5.4.3 describes the simulation and correction of the trigger bias in the Monte Carlo study. After determining N_4^W with the Berends Scaling method, the number of W + $\geqslant$ 4 jet in the biased sample, $\tilde{N}_4^W$ is obtained by:

$$\tilde{N}_4^W = N_4^W \cdot \varepsilon^{W+\geqslant 4 \text{ jets}},$$

where $\varepsilon^{W+\geqslant 4 \text{ jets}}$ is obtained from Monte Carlo.

5.4 Monte Carlo Study of the Berends Scaling

As part of the Monte Carlo study of measuring the $t\bar{t}$ production cross, the Berends scaling method is implemented using simulated events. First of all a sample containing $t\bar{t} \rightarrow \mu +$ jets and W + jets events is defined. The number of used Monte Carlo events is fixed, thus different integrated luminosities are simulated by scaling the number of events. The statistical fluctuations are given by the real size of the Monte Carlo sample, but the calculations of statistical uncertainties are done with respect to the simulated luminosity. The Monte Carlo study is performed for different simulated $t\bar{t}$ production cross sections. The correction of the trigger bias is simulated and the Berends scaling fit is applied. In the next section the obtained numbers of W + jets and $t\bar{t} \rightarrow \mu$+jets events in the fourth jet multiplicity bin are further used for the topological analysis.

5.4.1 W + jets Monte Carlo Samples

To study the Berends scaling with simulated events, a W + jets sample with different jet multiplicities n is necessary. The number N of events with n jets and the number M

of events with m jets have to be inter-normalized by their cross sections:

$$\frac{N}{M} = \frac{\sigma(W + n \text{ jets})}{\sigma(W + m \text{ jets})}.$$

However, it is difficult to create such a sample. If only one sample with all jet multiplicities was generated, the statistics for the W + 4 jets events would be too low compared to a reasonable W + 1 jet statistics because of the Berends scaling. Therefore, the used Monte Carlo event generator *ALPGEN* creates W + n jets events in n different samples. The generator calculates amplitudes for all W + n jet final states at leading order. Initial and final state radiation are not treated with QCD calculations, but with the parton showering model of *JETSET/PYTHIA*. A procedure is needed to obtain a well defined normalization for all samples. Since the parton showering may produce additional jets to the matrix element jets, events of a W + n jets sample can contain more then n jets. Therefore, simply adding all samples with respect to their cross section, calculated with amplitudes, would end in double counting of events. For example, a W + 1 jet event with one additional parton shower jet has to be inter-normalized with the W + 2 jets cross section and not with the W + 1 jets cross section, although it was originally generated as a W + 1 jet event be *ALPGEN*. The assignment of each event to the correct cross section can be achieved by investigating the events at Monte Carlo parton level. A W + n jet event without parton showering, i.e. the output of *ALPGEN*, contains by construction exactly n partons with $p_t > 12$ GeV, $|\eta| < 2.7$, and a distance between each couple of partons of $\Delta R(\text{parton}_i, \text{parton}_j) > 0.4$. These requirements are chosen for the Monte Carlo generation. For events with parton showering a simple algorithm counts the number of partons, that fulfill the same requirements. Unfortunately, not all information of all Monte Carlo particles and their history is stored in the Monte Carlo tree. In the following analysis, a W + n jets event ($n = 1 \ldots 3$) is defined as an event of the W + n jets *ALPGEN* sample, where the counting algorithm finds exactly n partons and n jets. Moreover, those n partons have to be spatially matched to the n reconstructed jets. The W + 4 jets sample contains $\geqslant 4$ partons found by the counting algorithm, that are matched to at least 4 jets. The impact of the parton cuts of the counting algorithm on the cross section measurement will be discussed in Section 6.3. Since not all partons arise from matrix elements the obtained samples cannot be normalized with calculated cross sections. Instead, they are normalized to measured DØ data. The results of the Berends scaling fit (Equation 5.4) obtained from data are [31, 29]:

$$N_1^W = 12979.4 \pm 319.4, \quad \alpha = 0.187 \pm 0.009. \tag{5.7}$$

For the analysis in [29] an integrated luminosity of $\mathcal{L} = 94\,\text{pb}^{-1}$ was available. The Monte Carlo samples are normalized with data, added, and finally scaled up to an integrated luminosity of $\mathcal{L} = 210\,\text{pb}^{-1}$. This value corresponds to the expected size of the DØ data sample that is being analyzed for the winter conferences 2004. Note, that the Berends scaling law cannot be tested with this Monte Carlo study, but is an assumption in the applied normalization procedure.

5.4.2 Signal Monte Carlo Sample

The simulated cross section is varied between 4 pb and 12 pb. This range includes the theoretical expectation of the cross section of about 7 pb and present measurements. As an example the next sections give intermediate results for a simulated cross section of 7 pb. The $t\bar{t} \to \mu +$ jets events are normalized to the simulated cross section σ and integrated luminosity $\mathcal{L} = 210\,\mathrm{pb}^{-1}$, i.e. the constant number of simulated $t\bar{t} \to \mu +$ jets events, $N_{t\bar{t}}^{\mathrm{MC}}$, is weighted by a factor

$$w_{\mathrm{norm}} = \frac{\sigma \cdot \mathcal{L} \cdot \mathrm{BR}}{N_{t\bar{t}}^{\mathrm{MC}}},$$

where BR is the branching ratio of the $t\bar{t} \to \mu +$ jets final state, i.e. 14.4 %.

5.4.3 Introducing and Correcting the Trigger Bias

The jet trigger bias is simulated by weighting each event with a factor w_{trig}, which is calculated using Equation 5.3. Afterwards, the weights of the W + jets and $t\bar{t} \to \mu +$ jets samples can be summed up to obtain the biased jet multiplicity distribution. The biased W+$t\bar{t}$ sample is the starting point of the Berends scaling method in the data analysis. First of all the bias has to be corrected by factors $1/\varepsilon_i^{W+t\bar{t}}$ according to Equation 5.6. As explained the biases $\varepsilon_i^{W+t\bar{t}}$ are measured with the single muon trigger that is independent from jets in an event. The data sample used to measure the biases is not the same as the preselected data sample taken for the analysis. Therefore, in the Monte Carlo study the biases $\varepsilon_i^{W+t\bar{t}}$ are measured in statistically independent samples. This means all simulated samples are divided in two parts. One half is used to measure efficiencies, the other half represents the data sample to be analyzed. Table 5.2 shows the $\varepsilon_i^{W+t\bar{t}}$ found in Monte Carlo. The uncertainties are obtained by varying the jet trigger

jet multiplicity i	$\geqslant 1$ jet	$\geqslant 2$ jets	$\geqslant 3$ jets	$\geqslant 4$ jets
ε_i^{W+tt}	$38.1 \pm 1.6\%$	$67.7 \pm 1.7\%$	$87.7 \pm 1.0\%$	$95.8 \pm 0.5\%$

Table 5.2: Trigger bias of the W+$t\bar{t}$ sample.

turn-on curve (Figure 5.5 (right)) by ± 1 GeV in the jet E_t. This is the same way the uncertainty of the jet trigger efficiency for simulated $t\bar{t} \to \mu + \geqslant 4$ jets is obtained (see Section 5.1.9). In the data analysis there is no systematic uncertainty of parameterizing the trigger turn-on curve, because this parameterization is not needed to measure the trigger bias. But the precision is limited by the statistics of the used data sample and systematics, e.g. due to the jet topology and flavor which might be different.

5.4.4 Berends Scaling Fit

Figure 5.9 shows the trigger bias corrected jet multiplicity distribution of the $W + t\bar{t}$ sample. In addition, the W + jets event fraction without signal is plotted. An integrated luminosity of $\mathcal{L} = 210\,\mathrm{pb}^{-1}$ is simulated and the $t\bar{t}$ production cross section is assumed to be 7 pb. Only in the fourth inclusive jet multiplicity bin the $t\bar{t} \to \mu +$ jets excess is visible. From normalizing the event numbers with the help of data the values of N_1^W,

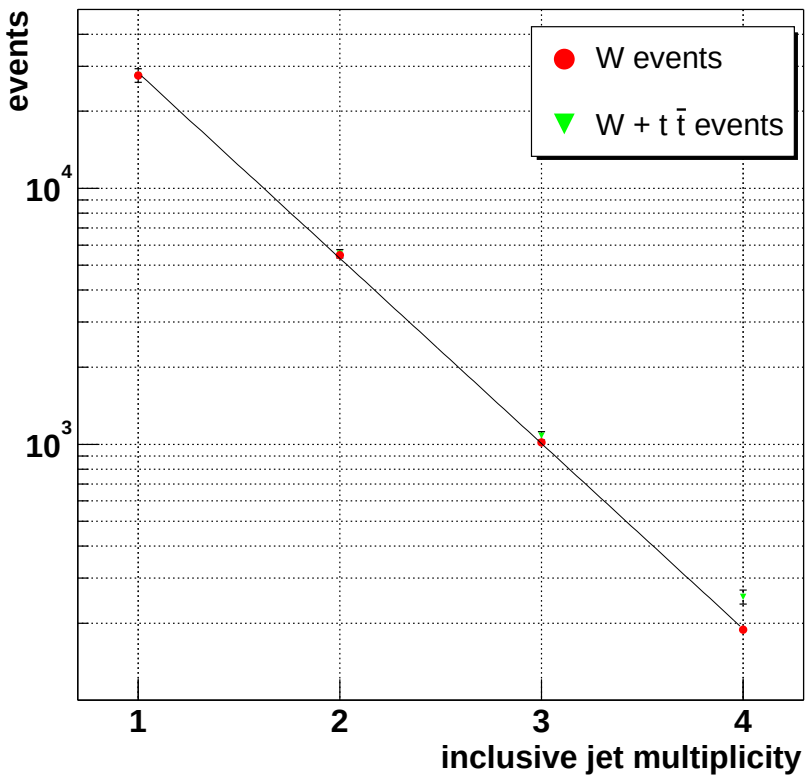

Figure 5.9: Jet multiplicity distribution of W + $t\bar{t}$ events and only W + jets events. The curve shows the W + jets subsample of the W + $t\bar{t}$ sample as a result of the Berends Scaling fit.

α, and N_4^W are known:

$$N_1^W = 28996.8, \qquad \alpha = 0.187, \qquad N_4^W = 189.6. \tag{5.8}$$

As explained in the previous section the trigger bias is introduced by weighting the events and it is corrected by factors $1/\varepsilon_i^{W+t\bar{t}}$. If the $\varepsilon_i^{W+t\bar{t}}$ were not determined in different samples than the simulated data samples, this would yield exactly the numbers

of Equation 5.8, again. But the statistical fluctuations in the jet E_t spectra lead to slightly different numbers in each bin:

$$N_1^W = 27593.6 \pm 1716.9, \qquad N_4^W = 188.2 \pm 14.3. \tag{5.9}$$

The uncertainties are calculated with error propagation taking the uncertainty of the number of unbiased events $\Delta\tilde{N}_i = \sqrt{\tilde{N}_i}$ and the bias corrections $\Delta\varepsilon_i^{W+t\bar{t}}$ (see Table 5.2) into account. Since the relative $t\bar{t}$ fraction in the first three bins is negligible, a preliminary estimation of the number of W events in the fourth jet multiplicity bin, N_4^W, can be obtained by fitting an exponential (Equation 5.10) to the first three bins and using the fit results to extrapolate the function to the fourth bin.

$$N_i^{W+t\bar{t}} = N_1^W \times \alpha^{i-1}. \tag{5.10}$$

The fit yields:

$$\text{fit (a):} \qquad N_1^W = 27847.0 \pm 1007.5, \qquad \alpha = 0.196 \pm 0.005.$$

With Equation 5.5 it follows that

$$N_4^W = 209.2 \pm 18.6.$$

Taking into account that all bins contain $t\bar{t} \to \mu +$jets events the distribution of all bins has to be fitted with Equation 5.4. In Table 5.3 the fractions $f_i^{t\bar{t}}$ of $t\bar{t} \to \mu +$jets events in each inclusive jet multiplicity bin i are given, as determined in Monte Carlo.

jet multiplicity i	$\geqslant$ 1 jet	$\geqslant$ 2 jets	$\geqslant$ 3 jets	$\geqslant$ 4 jets
$f_i^{t\bar{t}}$	100.0%	99.1%	90.4%	60.5%

Table 5.3: Fraction $f_i^{t\bar{t}}$ of $t\bar{t} \to \mu +$ jets events in each inclusive jet multiplicity bin.

The fit with Equation 5.4 results:

$$\text{fit (b):} \qquad N_1^W = 28034.2 \pm 1062.7, \qquad \alpha = 0.188 \pm 0.008 \qquad \Rightarrow \qquad N_4^W = 187.4 \pm 24.9.$$

The numbers in fit (b) are taken as parameters for Equation 5.10 and plotted in Figure 5.9. Table 5.4 summarizes all numbers and gives the relative uncertainties of N_4^W. Fit (a) is a good estimate on N_4^W, but always overestimates it as a consequence of neglecting the $t\bar{t} \to \mu +$ jets events in the first three bins. The uncertainties of fit (b) are dominated by the uncertainties of the trigger bias $\Delta\varepsilon_i^{W+t\bar{t}}$. To show the effect of the statistical uncertainty coming from $\Delta\tilde{N}_i$, Table 5.4 also lists the result of a third fit, where the uncertainty from the trigger bias is set to zero ($\Delta\varepsilon_i^{W+t\bar{t}} = 0$). The only reason for not obtaining the exact simulated values is a small difference from statistical fluctuations in the $t\bar{t}$ fractions, $f_i^{t\bar{t}}$, in the simulated data and the $f_i^{t\bar{t}}$ from Table 5.3 used for the fit. For the further analysis the results are taken from fit (b). In comparison to the *Lepton Photon Conference 2003* [31] results the measurement is a bit worse despite a higher luminosity, due to the uncertainties of $\Delta\varepsilon_i^{W+t\bar{t}}$.

	N_1^W	α	N_4^W	ΔN_4^W [%]
simulated values	28996.8	0.187	189.6	
after bias correction	27593.6±1716.9	-	188.2±14.3	7.6
fit (a)	27847.0±1007.5	0.196±0.005	209.2±18.6	8.9
fit (b)	28034.2±1062.7	0.188±0.008	187.4±24.9	13.3
$\Delta\varepsilon^{\text{bias}} = 0$	28996.9± 270.3	0.187±0.004	189.6±12.2	6.4
data (94 pb^{-1}) [31]	12979.4± 319.4	0.187±0.009	84.7±11.1	13.1

Table 5.4: Simulated values of the numbers of W + jets events and the results of different fits based on Berends Scaling. The first line gives the true simulated values. See text for the different results. In the last line the data results of the *Lepton Photon Conference 2003* [31] are given.

5.5 Topological Analysis of $\sigma(t\bar{t} \to \mu + \text{jets})$

The final analysis step is a topological selection of the events in the biased tight sample with four or more jets. So far, only muon properties, $\not{E}_t$, and jet multiplicities were used to select W + jets events. The so-called topological analysis relies on the topological characteristics of the whole event, which are different for signal and background events.

5.5.1 Topological Variables

With the help of three variables the background is further rejected. The topological selection is taken from the *Lepton Photon Conference 2003* [31] analysis:

- The first variable is the E_t of the leading jet. $t\bar{t} \to \mu + \text{jets}$ events contain jets in the central detector region with large transverse energy. In Figure 5.10 (a) it can be seen that the leading jet of W + jets events is on average softer than a leading jet of a $t\bar{t} \to \mu + \text{jets}$ event. This is due to the fact that the jets of W + jet events are mainly produced by collinearly radiated gluons of initial and final state radiation. The position of the cut is also marked:

$$\text{jet } E_t > 60 \text{ GeV}$$

- The second variable is called H_t. It is defined as the scalar sum of transverse energy of all jets within $|\eta| < 2.5$ and jet $E_t > 15$ GeV plus the reconstructed E_t of the leptonically decaying W boson:

$$H_t = E_t^W + \sum_{\text{jets}} \text{jet } E_t.$$

Figure 5.10 (b) shows the signal and background distribution. Signal events have a large H_t, due to the high mass of the produced $t\bar{t}$ pair. The topological cut is:

$$H_t > 250 \text{ GeV}.$$

- Another way to distinguish signal from background events is to look at the directions and momenta, $\vec{p^o}$, of all reconstructed objects o of an event. For this purpose a normalized momentum tensor is defined:

$$\mathcal{M}_{ij} = \frac{\sum_o p_i^o p_j^o}{\sum_o |\vec{p^o}|^2},$$

where i, j denote the Cartesian components of the momenta $\vec{p^o}$. 3/2 of the smallest eigenvalue of $\mathcal{M}$ is called aplanarity $\mathcal{A}$. It is a measure for the flatness of an event. $t\bar{t} \to \mu +$ jets events are more likely to have a spherical symmetry, whereas W + jets events are rather flat (see Figure 5.10 (c)). The spherical symmetry is typical for products of the decay of heavy particles, and the flatness of W + jets events arises from the high cross section of gluons to be radiated collinearly. Therefore, the following cut is applied:

$$\mathcal{A} > 0.05.$$

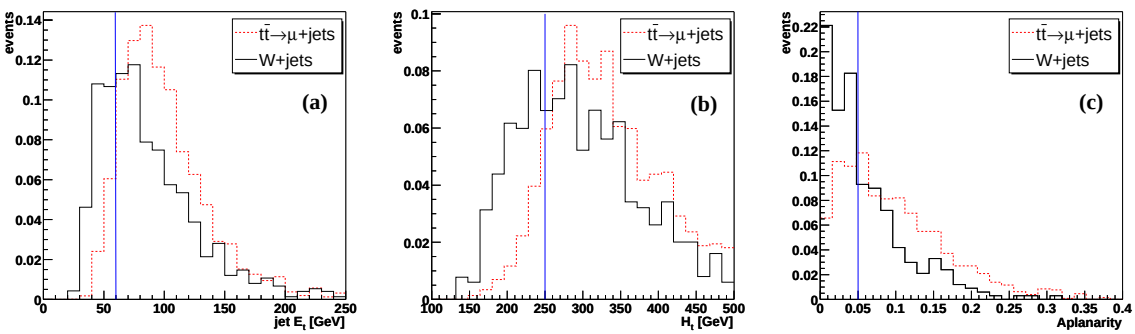

Figure 5.10: Distributions of the three topological variables for $t\bar{t} \to \mu +$ jets signal (dotted lines) and W + jets background (full line) and the applied cut positions. The plots (a), (b), and (c) show the leading jet E_t spectrum, the H_t distribution, and the aplanarity distribution, respectively.

The efficiencies for all topological cuts are determined with simulated events for signal and W + jets events, listed in Table 5.5. For a data analysis the efficiency for QCD events has to be measured, because the tight sample might still contain QCD background. It can be measured in a QCD data sample. The efficiency of the topological cuts for W

+ jets events and QCD events is very similar, as can be seen in the *Lepton Photon Conference 2003* [31] analysis. Hence, it is not important to know the ratio of W + jets and QCD background events.
Note, that the efficiencies for the W + jets sample depends on the applied parton cuts, that are described in Section 5.4.1. The stronger the parton cuts, the more efficient the topological cuts for the background. This systematic effect will be discussed in the next chapter.

	$t\bar{t} \to \mu+ \geqslant 4$ jets	W + $\geqslant 4$ jets
jet $E_t > 60$ GeV	$90.8 \pm 1.2\%$	$73.0 \pm 1.7\%$
$H_t > 250$ GeV	$88.1 \pm 1.4\%$	$70.2 \pm 1.9\%$
aplanarity > 0.05	$70.8 \pm 2.1\%$	$39.3 \pm 2.4\%$
$\varepsilon_{\text{topo}}$	$56.6 \pm 2.0\%$	$20.2 \pm 1.4\%$

Table 5.5: Efficiencies of the topological cuts on $t\bar{t} \to \mu+ \geqslant 4$ jets and W + $\geqslant 4$ jets events.

5.5.2 Simulation of the Topological Analysis of $\sigma(t\bar{t} \to \mu + \text{jets})$

The tight $W + t\bar{t}$ sample with four or more jets contains $N_4^{W+t\bar{t}} = 250.6$ events. $N_4^W = 187.4 \pm 24.9$ of them are estimated to be background. After the topological analysis there are $N_{\text{obs}} = 55.4$ events observed. The expected background fraction can be calculated with the efficiency for background:

$$N_{\text{bkg}} = \epsilon_{\text{topo}}^W \cdot N_4^W = 35.3.$$

The probability to observe N_{obs} events given the cross section is Poisson distributed. N_{obs} is sufficiently large, thus its uncertainty is given by:

$$\Delta N_{\text{obs}} = \sqrt{N_{\text{obs}}}.$$

5.6 Cross Section Measurement

The $t\bar{t}$ production cross section is obtained using the following equation:

$$\sigma(t\bar{t}) = \frac{N_{\text{obs}} - N_{\text{bkg}}}{\text{BR} \cdot \varepsilon \cdot \mathcal{L}}. \tag{5.11}$$

The overall efficiency ε of all cuts and requirements is the product of the preselection efficiency (Table 5.1) and the efficiency of the topological selection (Table 5.5) for signal events:

$$\varepsilon = \varepsilon_{\text{preselection}} \times \varepsilon_{\text{topo}} = 10.8 \pm 0.5\%.$$

Quantity	Value
N_{obs}	55.4 ± 7.4
N_{bkg}	35.3 ± 5.3
BR	14.4 %
ϵ	$10.8 \pm 0.5\%$
$\mathcal{L}$	210 pb^{-1}

Table 5.6: Summary of all quantities that enter the cross section.

All necessary quantities are determined and summarized in Table 5.6. Remember, that the values of N_{obs} correspond to a simulated $t\bar{t}$ production cross section of 7 pb. The measured cross section is found to be:

$$\sigma(t\bar{t}) = 6.1 \pm 2.3 \text{ (stat) pb.}$$

The statistical uncertainty of the cross section is a consequence of the uncertainty of N_{obs}. All other uncertainties are considered in the discussion of the systematics in the next chapter. Table 5.7 gives the results for all simulated cross sections. The measured cross sections are different from the simulated cross sections because there are different statistical fluctuations in the samples used to determine the efficiencies and the number of signal events. All measurements are 100 % correlated thus all measured cross sections are smaller than the simulated cross sections. If the measurements were statistically independent, positive and negative fluctuations of the measurement around the simulation would be expected. The relative uncertainty of the cross section decreases with increasing cross section, because N_{obs} increases linearly, but its uncertainty ΔN_{obs} increases only with the square root $\sqrt{N_{\text{obs}}}$.

simulated $\sigma(t\bar{t})$ [pb]	measured $\sigma(t\bar{t})$ [pb]	$\Delta\sigma(t\bar{t})$ (stat) [pb]	$\Delta\sigma(t\bar{t})/\sigma(t\bar{t})$ [%]
4.0	2.8	2.1	73.6
5.0	3.9	2.1	54.2
6.0	5.0	2.2	43.8
7.0	6.1	2.3	37.0
8.0	7.2	2.3	32.3
9.0	8.3	2.4	28.8
10.0	9.4	2.5	26.1
11.0	10.5	2.5	23.9
12.0	11.6	2.6	22.2

Table 5.7: The simulated and measured cross sections in pb for $t\bar{t}$ production and the absolute and relative statistical uncertainty for a simulated data sample of $\mathcal{L} = 210$ pb^{-1}.

6 Study of Systematic Uncertainties

In this chapter the sources of systematic uncertainties of the cross section are discussed. The main uncertainties are quantified within the Monte Carlo study.

6.1 Background, Efficiency, and Luminosity

The cross section is determined using Equation 5.11. ΔN_{obs} yields the statistical uncertainty. All other quantities contribute to the systematics:

- The number of background N_{bkg} has been estimated to be 35.3 ± 5.3. Remember, that only the W + jets background is simulated and estimated in the Monte Carlo study, but not the QCD background (see Section 3.3.2).
- The efficiency is: $\varepsilon = 10.8 \pm 0.5\,\%$. Here, the estimated uncertainty takes the statistical uncertainties of the efficiencies of all cuts and the systematic estimation of the uncertainties of trigger curves into account. Other effects like contributions from the uncertainty of the jet energy scale are discussed below.
- The results of the recently updated uncertainty of the luminosity measurements [35] is used: $\Delta\mathcal{L} = 6.5\,\% \cdot \mathcal{L}$. This uncertainty leads to a 6.5 % uncertainty of the cross section. At the *Lepton Photon Conference 2003* [31] the luminosity was only known to ±10 %. The precision of the measurement of the luminosity is limited by the exactness of the knowledge of geometrical acceptance of the luminosity counters and the measurement of the inelastic proton anti-proton scattering cross section.

The contribution to the uncertainty of the cross section is obtained with Gaussian error propagation. Table 6.2 shows the results.

6.2 Jet Energy Scale

The calibration of jet energies with the help of the jet energy scale, JES, (see Section 4.1.1) is one of the main sources of the systematic uncertainty in the data analysis as well as in the Monte Carlo study. The JES correction changes not only the jet E_t distribution,

	$\Delta\sigma$ [pb]	$\Delta\sigma/\sigma$ [%]
ΔN_{bkg}	1.6	26 %
$\Delta\mathcal{L}$	0.4	6.5 %
$\Delta\varepsilon$	0.3	4.6 %

Table 6.1: Systematic uncertainties of the cross section arising from N_{bkg}, $\mathcal{L}$, and ε. The simulated and measured cross section is 7.0 pb and 6.1 pb, respectively.

simulated $\sigma(t\bar{t})$ [pb]	measured $\sigma(t\bar{t})$ [pb]	$\Delta\sigma(t\bar{t})$ (syst) [pb]	$\Delta\sigma(t\bar{t})/\sigma(t\bar{t})$ [%]
7.0	6.1	1.7	27.6

Table 6.2: Systematic uncertainty of the measured cross section arising from the background estimation, the statistical uncertainty of the efficiency, and the uncertainty of the luminosity.

but also the jet multiplicity distribution due to the jet $E_t > 15$ GeV cut. In addition, the missing transverse energy, the muon isolation, and the topological variables are affected. The jet triggers remain unchanged, because the JES is an offline correction to events that already passed the triggers. However, in order to measure the trigger efficiencies the parameterized trigger curves are convoluted with simulated jet spectra, which depend on the JES. Thus, the JES impacts also the jet trigger efficiency and the trigger bias corrections. In the Monte Carlo study the number of events in each multiplicity bin is fixed by the normalization. If all quantities were determined by data, the effect of a mismeasured JES would cancel when calculating the cross section, because the estimated number of signal and background events would be affected in the same way as the efficiencies. However, some quantities are determined in the simulation. Differences in the Monte Carlo JES and data JES lead to an uncertainty of the cross section. To estimate this effect, all quantities which are measurements with the simulation are repeated varying the JES by $\pm\Delta$JES, where ΔJES is the combined statistical and systematic uncertainty of the JES. In the Monte Carlo study this is also done, but the Monte Carlo sample representing the data remains unchanged. For the JES variation the Monte Carlo JES uncertainty is used. Table 6.2 shows all signal efficiencies, that depend on the JES. The values in the second column are taken from Table 5.1 and Table 5.5. In the third and fourth column the recalculated values with varied JES are given. With the new values of the efficiencies the cross section measurement is repeated yielding the two new cross sections $\sigma(\text{JES} + \Delta\text{JES})$ and $\sigma(\text{JES} - \Delta\text{JES})$. The systematic uncertainty of the cross section caused by the uncertainty of the JES is calculated using:

$$\Delta\sigma^{\pm}_{\text{JES}} = |\sigma(\text{JES} \pm \Delta\text{JES}) - \sigma(\text{JES})|.$$

Efficiency	unchanged	$+\Delta$JES	$-\Delta$JES
$\varepsilon^{\mu}_{\text{isolation}}$	90.2 ± 0.8 %	$90.2 \pm 0.8\%$	$90.1 \pm 0.8\%$
$\varepsilon_{\text{Njets}} \times \varepsilon^{\text{jet}}_{\text{ID}}$	62.1 ± 0.8 %	63.9 ± 0.8 %	$60.2 \pm 0.8\%$
$\varepsilon^{\text{jet}}_{\text{trigger}}$	99.7 ± 0.1 %	99.8 ± 0.04 %	$99.4 \pm 0.1\%$
$\varepsilon_{\not{E}_t}$	90.9 ± 1.1 %	90.7 ± 1.1 %	$90.5 \pm 1.2\%$
$\varepsilon_{\text{preselection}}$	$19.2 \pm 0.6\%$	$19.8 \pm 0.6\%$	$18.2 \pm 0.6\%$
$\varepsilon_{\text{jet}E_t}$	$90.8 \pm 1.2\%$	$93.6 \pm 1.0\%$	$86.4 \pm 1.5\%$
ε_{H_t}	$88.1 \pm 1.4\%$	$91.1 \pm 1.2\%$	$85.3 \pm 1.6\%$
$\varepsilon_{\text{apla}}$	$70.8 \pm 2.1\%$	$71.7 \pm 2.0\%$	$70.4 \pm 2.2\%$
$\varepsilon_{\text{topo}}$	$56.6 \pm 2.0\%$	$61.2 \pm 2.0\%$	$51.9 \pm 2.1\%$
$\varepsilon_{\text{total}}$	$10.8 \pm 0.5\%$	$12.1 \pm 0.6\%$	$9.5 \pm 0.5\%$

Table 6.3: Signal efficiencies of all cuts, that depend on the jet energy scale. The last two columns give the recalculated efficiencies with varied jet energy scale by $\pm\Delta$JES.

Table 6.4 lists the results for the JES variation.

simulated $\sigma(t\bar{t})$ [pb]	measured $\sigma(t\bar{t})$ [pb]	$\Delta\sigma^{+}_{\text{JES}}$ [pb]	$\Delta\sigma^{+}_{\text{JES}}/\sigma$ [%]	$\Delta\sigma^{-}_{\text{JES}}$ [pb]	$\Delta\sigma^{-}_{\text{JES}}/\sigma$ [%]
7.0	6.1	0.50	8.2	2.1	34.9

Table 6.4: Systematic uncertainty of the cross sections due to the JES.

The asymmetry of the uncertainty emerges from cuts on distributions which are not flat. For example, the cut on the exponentially decreasing distribution of the jet E_t causes very different event selections and efficiencies depending on whether the JES is varied in the positive or negative direction. Moreover, there is a large statistical uncertainty of the estimation of the systematics due to the size of the W + jets Monte Carlo sample used to determine the efficiencies of the topological variables and the trigger bias correction. The large difference between the measured cross section $\sigma = 6.1$ pb and the cross section $\sigma^{-}_{\text{JES}} = 8.2$ pb obtained with varied JES is dominated by the W + jets background estimation. In the data analysis presented at the *Lepton Photon Conference 2003* [31] the systematic uncertainty arising from the JES was estimated to +15.2 % -16.6%. There are great efforts to reduce this uncertainty.

6.3 Parton Cuts

A description of the modeling of the W + jets events is given in Section 5.4.1. The W + jets events are generated with the following requirements on the partons created in the hard scattering process ("first modeling"):

$$p_t > 12 \text{ GeV} \qquad |\eta| < 2.7 \qquad \Delta R(\text{parton i, parton j}) > 0.4.$$

The jet multiplicities of the events after the parton showering is determined by counting the number of partons, that pass these cuts. Moreover, the partons are spatially matched to reconstructed jets. Hence, every W + n jets events contains n partons with at least 12 GeV. It was mentioned that these cuts impact the efficiencies of the topological cuts and the jet trigger bias. To estimate the effect of the modeling of the W + jets background, the cross section measurement is repeated with a second way of modeling the W + jets background. The same generated events with the same parton cuts are used, but this time there are no further parton level requirements after the parton showering. To determine the jet multiplicity only the jet parton matching is used. Figure 6.1 shows the tranverse energy spectrum of the leading jet (Figure 6.1 (a)) and the H_t distribution (Figure 6.1 (b)) for both ways of modeling the W + jets background. The distribution for the events with parton cuts after the parton showering have on average a larger transverse jet energy and a larger H_t. As a consequence, the efficiencies of the topological selection are different. They are given in Table 6.5 The differences in

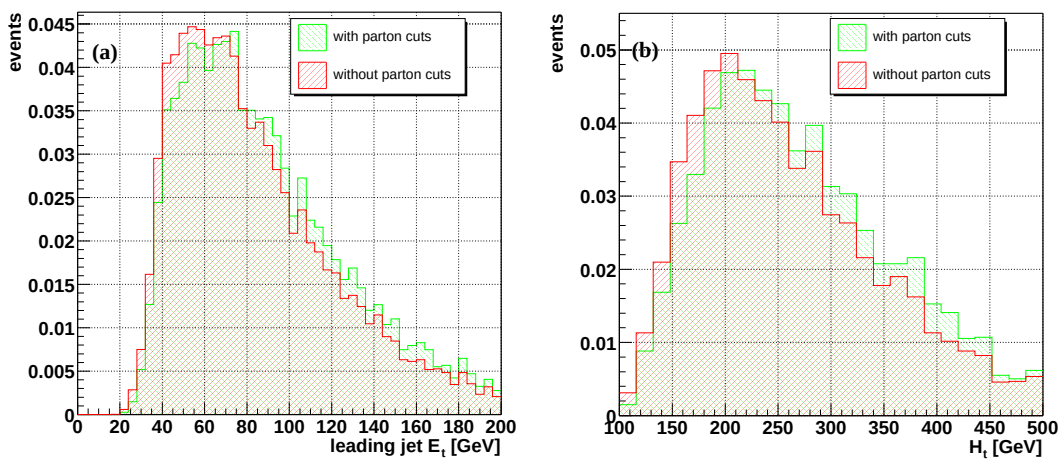

Figure 6.1: Leading jet E_t (a) and H_t (b) for simulated W + *geqslant* 4 jets events with and without parton cuts after the parton shower simulation.

	W + $\geqslant$ 4 jets with parton cuts	W + $\geqslant$ 4 jets without parton cuts
jet $E_t > 60$ GeV	$73.0 \pm 1.7\%$	$68.2 \pm 1.4\%$
$H_t > 250$ GeV	$70.2 \pm 1.9\%$	$65.1 \pm 1.6\%$
aplanarity > 0.05	$39.3 \pm 2.4\%$	$34.9 \pm 1.9\%$
$\varepsilon_{\text{topo}}$	$20.2 \pm 1.4\%$	$15.5 \pm 1.0\%$

Table 6.5: Efficiencies of topological cuts with and without parton cuts after the parton showering.

simulated $\sigma(t\bar{t})$ [pb]	measured $\sigma(t\bar{t})$ [pb] (1. modeling)	measured $\sigma(t\bar{t})$ [pb] (2. modeling)
7.0	6.1	7.5

Table 6.6: Cross section measurement for two different ways of modeling the W + jets background (see text).

the cross sections is obtained in both ways of modeling the background estimates the systematic uncertainty. The result is given in Table 6.6.

The relaxed requirements of the assignment of events to the W + jets samples increases the available statistics. Due to the smaller efficiency of the topological selection of the W + 4 jets background there is a better signal to background ratio. This leads to a smaller difference between the simulated cross section (7.0 pb) and the measured cross section (7.6 pb). However, it is not clear which of the two methods is more correct. Therefore, the difference in the measured cross section determined with both methods is taken as a conservative estimate on the cross section uncertainty coming from the W + jets modeling. This leads to an uncertainty of 23.4 %. The data analysis makes only use of a W + $\geqslant$ 4 jets sample. The difficulty of adding events with one, two and three jets does not arise, thus the systematic uncertainty is smaller.

6.4 Summary of the Systematic Uncertainties

All estimated uncertainties are summarized in Table 6.7. The combined systematic uncertainty is obtained by:

$$(\Delta\sigma)_{\text{syst}}(t\bar{t}) = \sqrt{\sum_i (\Delta\sigma)_i^2}.$$

	$\Delta\sigma/\sigma$ [%]
ΔN_{bkg}	$\pm$ 26.4
$\Delta\varepsilon$ (stat.)	$\pm$ 4.6
$\Delta\mathcal{L}$	$\pm$ 6.5
$\pm\Delta$JES	+34.9 -8.2
MC modeling	$\pm$ 23.4

Table 6.7: Summary of all estimated systematic uncertainties.

Figure 6.2 shows the measured versus the simulated cross section with the statistical and the total uncertainty:

$$(\Delta\sigma)_{\text{total}} = \sqrt{(\Delta\sigma_{\text{stat}})^2 + (\Delta\sigma_{\text{syst}})^2}.$$

The cross section is varied between 4 pb and 12 pb. Since the different cross sections are simulated by scaling the number of signal events, all entries in Figure 6.2 are 100% correlated. The absolute uncertainty increases slightly with increasing simulated cross section while the relative uncertainty decreases.

6.5 Other Systematic Uncertainties

The discussion of systematic uncertainties of the $\sigma(t\bar{t} \to \mu + \text{jets})$ cross section measurement is not complete but contains only the largest uncertainties. Besides the jet energy scale there is an uncertainty arising from the jet resolution. To study the jet energy resolution, the jet E_t distribution can be smeared, i.e. the resolution is determinate. The uncertainty of the top quark mass causes another systematic effect. Varying the top mass in the Monte Carlo events by its uncertainty allows to study the impact on the cross section measurement. For a full discussion of the systematics of the data analysis, see [29].

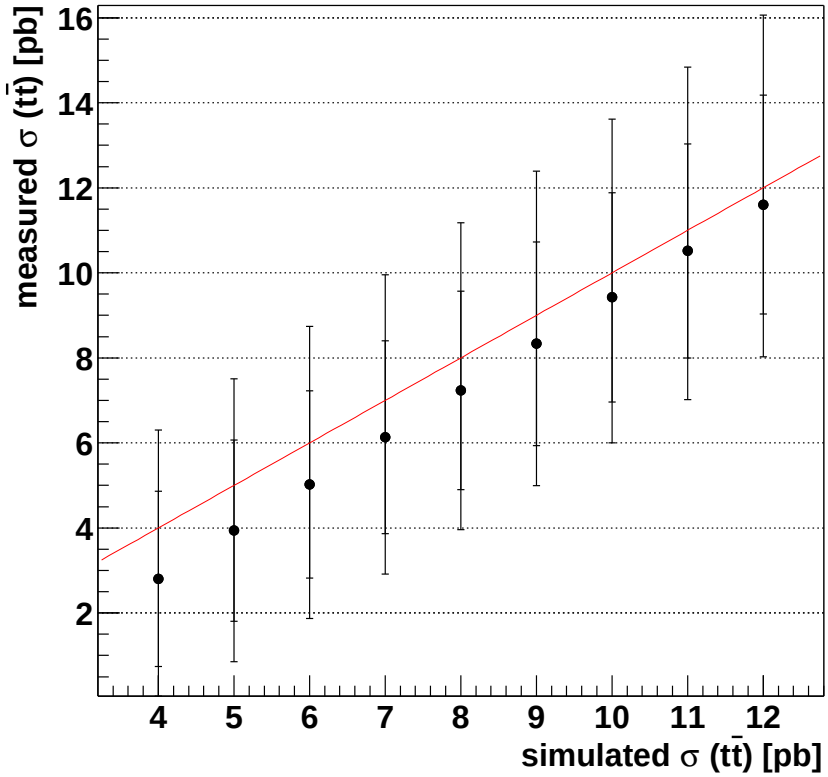

Figure 6.2: Measured vs. simulated cross section in the range between 4 pb and 12 pb. The obtained values are 100% correlated.

7 Summary and Outlook

The physics of the top quark is an interesting subject to study. After the top quark discovery in Run I, the Run II analyses try to increase the precision of the results and to perform new tests on the Standard Model. At present, the analyzed amount of Run II data is comparable to Run I, but soon there will be analyses with much larger statistics. In order to increase the precision of the measurement of the top production cross section also the systematic effects have to be better understood and further reduced. This thesis has presented the steps of the analyses in the muon + jets channel. The Monte Carlo studies have investigated and confirmed several methods which are later applied to the data. Such studies with simulations help to understand and improve these methods, that allow to measure most quantities independent from simulations, which is essential at hadron collider experiments. Finally, the uncertainty on a cross section measurement with 210 pb^{-1} is determined. This can be partially seen as an estimation of the results that will be expected for the next winter conferences.
There will be several improvements in future cross section analyses. They will profit from better object identifications. While finishing this thesis a new muon reconstruction version has been certified with a higher identification efficiency. More detector information will be read out and used. There exists an alternative method to the Berends Scaling to estimate the W + jets background, which is similar to the matrix method, but uses topological properties as tight criteria. This method does not have to correct the jet trigger bias and does not rely on the assumption on the Berends Scaling law. In order to reduce the uncertainty due to the jet energy scale new topological variables are investigated that depend less on the jet energy scale. There will be new optimizations of all cuts in order to minimize the statistical and systematic uncertainty of the cross section [32].

Bibliography

[1] S. L. Glashow, "Partial Symmetries of Weak Interactions," *Nucl. Phys.* **22** (1961) 579–588.

[2] S. Weinberg, "A Model of Leptons," *Phys. Rev. Lett.* **19** (1967) 1264–1266.

[3] A. Salam, "Elementary Particle Physics." N. Svartholm, ed., Nobel Symposium No. 8, Almqvist & Wiksell, Stockholm, 1968.

[4] P. W. Higgs, "Broken Symmetries, Massless Particles and Gauge Fields," *Phys. Lett.* **12** (1964) 132–133.

[5] F. Englert and R. Brout, "Broken Symmetry and the Mass of Gauge Vector Mesons," *Phys. Rev. Lett.* **13** (1964) 321–322.

[6] G. S. Guralnik, C. R. Hagen, and T. W. B. Kibble, "Global Conservation Laws and Massless Particles," *Phys. Rev. Lett.* **13** (1964) 585–587.

[7] D. J. Griffiths, *Introduction to Elementary Particles.* New York, USA: Wiley (1987) 392p.

[8] **CDF** Collaboration, F. Abe *et al.*, "Observation of Top Quark Production in anti-p p Collisions," *Phys. Rev. Lett.* **74** (1995) 2626–2631, `hep-ex/9503002`.

[9] **D0** Collaboration, S. Abachi *et al.*, "Observation of the Top Quark," *Phys. Rev. Lett.* **74** (1995) 2632–2637, `hep-ex/9503003`.

[10] Demortier, L. et al., "Combining the Top Mass Results from Run 1 from CDF and D0." FERMILAB-TM-2084, 1999.

[11] S. Willenbrock, "Studying the Top Quark," *Rev. Mod. Phys.* **72** (2000) 1141–1148, `hep-ph/0008189`.

[12] M. J. G. Veltman, "Second Threshold in Weak Interactions," *Acta Phys. Polon.* **B8** (1977) 475.

[13] **LEP** Collaboration, "Electroweak Parameters of the Z0 Resonance and the Standard Model: the LEP Collaborations," *Phys. Lett.* **B276** (1992) 247–253.

[14] **LEP** Collaboration, "A Combination of Preliminary Electroweak Measurements and Constraints on the Standard Model," `hep-ex/0312023`.

[15] **CTEQ** Collaboration, H. L. Lai *et al.*, "Global QCD Analysis of Parton Structure of the Nucleon: CTEQ5 Parton Distributions," *Eur. Phys. J.* **C12** (2000) 375–392, `hep-ph/9903282`.

[16] N. Cabibbo, "Unitary Symmety and Leptonic Decays," *Phys. Rev. Lett.* **10** (1963) 531–532.

[17] M. Kobayashi and T. Maskawa, "CP Violation in the Renormalizable Theory of Weak Interaction," *Prog. Theor. Phys.* **49** (1973) 652–657.

[18] **Particle Data Group** Collaboration, K. Hagiwara *et al.*, "Review of Particle Physics," *Phys. Rev.* **D66** (2002) 010001.

[19] F. A. Berends, W. T. Giele, H. Kuijf, R. Kleiss, and W. J. Stirling, "Multi - Jet Production in W, Z Events at p anti-p Colliders," *Phys. Lett.* **B224** (1989) 237.

[20] F. B. Division, "RunII Handbook." Fermilab Beams Division RunII Webpage, http://www-bd.fnal.gov/runII/index.html.

[21] **The D0** Collaboration, S. Abachi, "The D0 Upgrade: The Detector and its Physics." FERMILAB-PUB-96-357-E, 1996.

[22] T. LeCompte and H. T. Diehl, "The CDF and D0 Upgrades for Run II," *Ann. Rev. Nucl. Part. Sci.* **50** (2000) 71–117.

[23] **The D0** Collaboration, S. Abachi, "The D0 Detector," *NIM* **A338** (1994) 185.

[24] M. L. Mangano, M. Moretti, F. Piccinini, R. Pittau, and A. D. Polosa, "ALPGEN, a Generator for Hard Multiparton Processes in Hadronic Collisions," *JHEP* **07** (2003) 001, `hep-ph/0206293`.

[25] T. Sjöstrand, L. Lönnblad, and S. Mrenna, "PYTHIA 6.2: Physics and Manual," `hep-ph/0108264`.

[26] T. Sjöstrand, "High-Energy Physics Event Generation with PYTHIA 5.7 and JETSET 7.4," *Comp. Phys. Comm.* **82** (1994) 74.

[27] R. Brun, R. Hagelberg, M. Hansroul, and J. C. Lassalle, "GEANT: Simulation Program for Particle Physics Experiments. User Guide and Reference Manual,". CERN-DD-78-2-REV.

[28] G. Blazey *et al.*, "Run II Jet Physics." DØ-Note 3750, April, 2002.

[29] M. Klute, *A Measurement of the $t\bar{t}$ Production Cross Section in Proton-Antiproton Collisions at $\sqrt{s} = 1.96$ TeV with the D0 Detector at the Tevatron.* Doktorarbeit, Rheinische Friedrich-Wilhelms-Universität Bonn, 2004.

[30] A. Schwartzman and M. Narain, "A New 3-Dimensional Cone Track-Clustering Algorithm." DØ-Note 3885, July, 2001.

[31] **The D0** Collaboration, S. Abachi, "Update of the Measurement of the $t\bar{t}$ Cross Section at $\sqrt{s} = 1.96$ TeV." FERMILAB-Conf-03/248-E, 2003.

[32] Top Group, "Measurement of the $t\bar{t}$ Production Cross Section at $\sqrt{s} = 1.96$ TeV in the Lepton+Jets Final States using a Topological Method." DØ-Note in preparation, 2004.

[33] Anderson, Barberis, Bassler, Beaudette, Bernardi, Cho, Clement, Demina, Fiedler, Gerber, Golling, Grivaz, Groer, Han, Heinson, Iashvili, Juste, Li, Kado, Kehoe, Khanov, Klute, Kozminski, Quadt, Quinn, Mal, O'Neil, Parua, Perea, Phaf, Rizatdinova, Schwartzman, Schwienhorst, Shabalina, Strandberg, Whiteson, Zielinski, and Zitoun, "Measurement of the $t\bar{t}$ Cross Section at $\sqrt{s} = 1.96$ TeV." DØ-Note 4116, March, 2003.

[34] T. Golling. private communication, 2004.

[35] T. Edwards, S. Yacoob, T. Andeen, J. Park, B. Casey, M. Begel, R. Partridge, H. Schellman, and A. Sznajder, "The Updated D0 Luminosity Determination." DØ-Note 4328, January, 2004.

[36] M. Klute, "Measurement of the $t\bar{t}$ Production Cross Section at $\sqrt{s} = 1.96$ TeV in the Mu+Jets Final State." DØ-Note 4185, August, 2003.

Acknowledgement

Diese Arbeit wäre nicht ohne die große Unterstützung vieler Personen möglich gewesen. Ich möchte mich sehr bei Prof. Dr. N. Wermes bedanken, dafür dass er mir das Arbeiten an einem interessanten Experiment auf dem Gebiet der Elementarteilchenphysik ermöglicht hat und mich durch meinen Fermilabaufenthalt maßgeblich gefördert hat. Ein herzlicher Dank gilt meinen Eltern und meiner Schwester Anja, die mich während meines gesamten Studiums unterstützt haben. Für die Betreuung und viele hilfreiche Erklärungen möchte ich mich besonders bei Dr. Arnulf Quadt bedanken. Ich profitierte von seinen Anregungen für meine Arbeit und vielen Diskussionen mit ihm. Mein weiterer Dank gilt Dr. Markus Klute, der mich während meiner Zeit am Fermilab und in der Endphase meiner Diplomzeit freundschaftlich betreute. Bei Prof. Dr. I. Brock bedanke ich mich für die freundliche Übernahme des Korreferats. Für die angenehme Arbeitsatmosphäre danke ich allen ehemaligen und aktiven Bonn-DØ-Mitgliedern: Tobias Golling, Dr. Markus Klute, Prof. Dr. M. Kobel, Kevin Kröninger, Su-Jung Park, Dr. Arnulf Quadt, Dr. Christian Schwanenberger, Markus Warsinsky und Prof. Dr. N. Wermes. Ausserdem danke ich allen Freunden, die mich privat und in der Physik während meiner Zeit im Studium begleitet haben.